Abiogenic amorphous silica: Ordering from the atomic to centimeter scale

A Dissertation

Submitted in Partial Fulfilment of the Requirements for the Degree of

Doktor der Naturwissenschaften (Dr. rer. nat.)

to the Department of Earth Sciences

of Freie Universität Berlin

by

Moritz Liesegang

Berlin, January 2018

Gutachter: PD Dr. Ralf Milke

Prof. Timm John

Prof. Oliver Plümper

Disputationsdatum: 02.05.2018

Erklärung der Eigenständigkeit

Hiermit versichere ich, dass ich die vorliegende Arbeit selbstständig verfasst und keine anderen als die angegebenen Quellen und Hilfsmittel benutzt habe; alle Ausführungen, die anderen Schriften wörtlich oder sinngemäß entnommen wurden, kenntlich gemacht sind und die Arbeit in gleicher oder ähnlicher Fassung noch nicht Bestandteil einer Studien- oder Prüfungsleistung war.

Berlin,

Table of contents

Summary

Chemical weathering of silicate minerals constitutes a principal component of the global silicon cycle and produces one of the fundamental building blocks of Earth's bio- and geosphere: nanoparticulate (<1 µm) amorphous silica (opal-A). Amorphous nanoparticles are ubiquitous in nature and have increasingly been identified as fundamental precursors for carbonate and phosphate crystal formation and growth processes in natural systems. However, only the inorganic amorphous-to-crystalline pathway of opal-A results in X-ray amorphous, three-dimensionally ordered arrays of uniform nanoparticles. Since the first micromorphological description of opal-A in the early 1960s it is widely assumed that growth and ordering of uniform silica spheres in sedimentary environments proceed via gel network formation and subsequent slow gravitational sphere settling at quiescent conditions. This fundamental assumption comprises amorphous silica in void-filling and replacement contexts, but lacks direct observational evidence. Similarly, the underlying processes of the early-diagenetic transformation of metastable opal-A toward more crystalline opaline phases are presently unexplained.

To investigate the processes that drive the amorphous silica system from a disordered to an ordered state, I use vein-filling and replacement silica collected from deeply chemically weathered sedimentary rocks of the Great Artesian Basin (central Australia). Using a combination of high-resolution electron microscopy, nanotomography, electron probe microanalysis, X-ray microdiffraction, and micro-Raman spectroscopy, I characterized precisely the structural state and chemical composition of inorganically precipitated amorphous silica. This thesis presents the underlying ordering mechanisms identified on the level of atomic and colloidal dimensions. These findings lead to new coherent models for amorphous silica ordering processes on a pathway from dispersed particles to single crystals.

Amorphous silica nanospheres replace dolomite and twinned calcite crystals in bivalve shells, extensional fractures, and cherts via an interface-coupled dissolution-precipitation process. Electron microscopy and nanotomography show that the resultant photonic crystals form by continuous nanoparticle nucleation, aggregation, and subsequent arrangement into face-centered cubic (fcc) sphere lattices. I demonstrate that close-packed lattice planes coincide with the thermodynamically most stable calcite faces, and conclude in a novel model that the replacement process proceeds via a nanoparticle-based, nonclassical crystallization route. Electron and transmitted light microscopy show that macroscopic characteristics of vein-filling opal directly link to flow-induced micromorphological features. The non-Newtonian flow induces structuring of concentrated colloidal suspensions and directional ordering of nonspherical particles. Post-depositional shear compacts periodic sphere arrays, decreases the wavelength of diffracted light, and generates dislocations along close-packed slip planes in fcc lattices. Highly resolved X-ray microdiffraction, heating experiments, and calculated diffractograms show that during early-stage diagenesis metastable opal-A transforms into opal-CT via nanoscale *in situ* nucleation and growth of low-tridymite/cristobalite domains. This process is decoupled from opal chemical and micromorphological

properties and begins significantly earlier than previous studies suggest. As these results demonstrate for the first time, the mineralogical early-stage transformation of opal-A is a gradual process traceable by systematic peak shifts and symmetry variations in X-ray diffraction patterns.

In conclusion, amorphous silica ordering results from particle flow, aggregation, and crystallization processes ranging from nanodomains at the atomic scale, to particles tens to hundreds of nanometers in size, and finally ordered lattices in the centimeter range. I find that subparticle aggregation in a sol is favored over gelling in void-filling and replacement contexts and present direct evidence for dynamic colloid ordering processes. The replacive interaction model introduced here covers solid-solid phase changes ranging from natural mineral interfaces to the controllable synthesis of three-dimensionally ordered materials; thus, it links the fields of geosciences and materials science. Using X-ray diffraction pattern asymmetry offers a valid, but so far underestimated approach to quantify the early-stage diagenesis of opal-A with a widely available analytical method. The implications of the early-stage crystallization processes identified here range from the diagenetic modification of the Si isotopic record on Earth to potential hosts for fossil life on Mars. Overall, this thesis provides novel, evidence-based concepts that challenge the classical theory of gel formation and slow gravity-driven particle ordering at quiescent conditions, prevailing in opal research for the past 50 years.

Zusammenfassung

Die chemische Verwitterung von Silikatmineralen ist ein Hauptbestandteil des globalen Silizium-Kreislaufs und resultiert in einem der fundamentalen Bausteine der Bio- und Geosphäre der Erde: Silica-Nanopartikel (<1 µm) aus amorphem, hydratisiertem SiO_2 (Opal-A). Amorphe Nanopartikel sind allgegenwärtig in der Natur und werden zunehmend als essenzielle Vorläufer für die Carbonat- und Phosphatkristallisation und anschließende Wachstumsprozesse in natürlichen Systemen identifiziert. Allerdings bilden nur abiogene Silica-Nanopartikel röntgenamorphe, dreidimensional-periodische Gitteranordnungen. Seit der ersten mikromorphologischen Beschreibung von Opal-A in den frühen 1960er Jahren wird angenommen, dass Wachstum und Ordnung uniformer Nanopartikel in sedimentären Umgebungen durch einen Gelierungsprozess und gravitative Ablagerung in einer stagnierenden Lösung ablaufen. Diese Annahme gilt für Hohlraumfüllungen und Pseudomorphosen. Bislang mangelt es jedoch an direkten Beobachtungen, um diesen elementaren Schritt im Silica-Bildungsprozess zu belegen. Ebenfalls ungeklärt sind die Prozesse, welche der frühdiagenetischen Umwandlung von metastabilem, amorphem Silica zu höherkristallinen opalinen Phasen zugrunde liegen.

Um die Prozesse zu untersuchen, die das röntgenamorphe Silicasystem von einem ungeordneten in einen geordneten Zustand überführen, untersuche ich in dieser Arbeit Opal-A Hohlraumfüllungen und Pseudomorphosen aus chemisch tiefenverwitterten Sedimentgesteinen des Great Artesian Basin (Zentralaustralien). Durch eine Kombination hochauflösender Elektronenmikroskopie, Nanotomographie, Elektronenstrahlmikrosondenanalytik, Mikroröntgenbeugung und Mikro-Ramanspektroskopie war es möglich, die Struktur und chemische Zusammensetzung von abiogenem, amorphem Silica präzise zu charakterisieren. Die vorliegende Arbeit zeigt auf, welche grundlegenden Ordnungsprozesse auf der atomaren und kolloidalen Skala identifiziert wurden. Diese Ergebnisse bilden die Grundlage für neue, kohärente Modelle der Ordnungsprozesse eines natürlichen, amorphen Materials, auf dem Weg von dispergierten Partikeln zu echten Einkristallen.

In Muschelschalen, Dehnungsrissen und Cherts ersetzen Silica-Nanosphären Dolomit und verzwillingten Calcit mittels eines grenzflächenkontrollierten Lösungs-Fällungs-Prozesses. Elektronenmikroskopie und Nanotomographie zeigen, dass während dieses Prozesses kristalline Strukturen durch kontinuierliche Nanopartikelnukleation, -aggregation und Anordnung in einer kubisch dichtesten Kugelpackung (fcc) gebildet werden. Die dichtest-gepackten Netzebenen dieser geordneten Partikelaggregate stimmen mit den thermodynamisch stabilsten Calcitflächen überein. Ich folgere in einem neuen Modell, dass der Ersetzungsprozess einem nanopartikel-basierten, nichtklassischen Kristallisationspfad folgt. Darüber hinaus zeigen Elektronen- und Durchlichtmikroskopie, dass die makroskopischen Eigenschaften von Opal-A Hohlraumfüllungen direkt mit strömungsinduzierten mikromorphologischen Merkmalen korrelieren. Nicht-Newtonsches Fließen verursacht eine Strukturierung von kolloidalen Lösungen und die Ausrichtung ellipsoider Partikel. Nach der Ablagerung führt eine Scherung zu einer

Kompaktion von regelmäßigen Nanopartikelanordnungen und der Wellenlängen-abnahme des an dem Partikelgitter gebeugten sichtbaren Lichts. Die Bildung von spannungsinduzierten Dislokationen erfolgt entlang der dichtest gepackten Gleitebenen im fcc-Gitter. Mikroröntgenbeugung mit hoher Ortsauflösung, Heizexperimente und modellierte Diffraktogramme zeigen, dass die frühdiagenetische Kristallisation von metastabilem Opal-A durch nanoskalige *in situ* Nukleation und das Wachstum von Tief-Tridymit/Cristobalit-Domänen erfolgt. Dieser Prozess ist entkoppelt von den chemischen und mikromorphologischen Eigenschaften des Opals und beginnt wesentlich früher, als bisherige Studien andeuten. Diese Ergebnisse zeigen erstmals, dass die frühdiagenetische mineralogische Umwandlung von amorphem Silica ein gradueller Prozess ist, der durch systematische Peakverschiebungen und Asymmetrieänderungen in Diffraktogrammen nachweisbar ist.

Die Ergebnisse dieser Arbeit zeigen, dass die Ordnung von amorphem Silica durch Partikelfließ-, Aggregations- und Kristallisationsprozesse verursacht wird. Diese Prozesse reichen von Nanodomänen auf atomarer Ebene, zu Partikeln im Zehner- bis Hunderter-Nanometerbereich und schließlich geordneten Gitterstrukturen im Zentimeterbereich. Basierend auf direkten Beobachtungen wird deutlich, dass ein Gelierungsprozess eher die Ausnahme als die Regel bei der Bildung und räumlichen Ordnung uniformer Silica-Nanopartikel darstellt. In den in dieser Arbeit identifizierten dynamischen Ordnungsprozessen spielt aggregatives Partikelwachstum in einer Kolloiddispersion eine weitaus bedeutendere Rolle. Dies gilt sowohl für Hohlraumfüllungen als auch für Pseudomorphosen. Das hier eingeführte nanopartikelbasierte Mineralersetzungsmodell zeigt die Rolle und Dynamik von Nanopartikeln in Ersetzungsreaktionen deutlich auf. Der potentielle Anwendungsbereich erstreckt sich von natürlichen Mineraloberflächen bis zur kontrollierten Synthese dreidimensional geordneter Materialien und verknüpft damit die Geowissenschaften mit den Materialwissenschaften. Auf der atomaren Skala zeigt sich, dass die Etablierung eines Asymmetrieparameters für Röntgendiffraktogramme von amorphem Silica einen bislang unterschätzten, vielversprechenden Ansatz darstellt, um dessen frühdiagenetische Kristallisation zu quantifizieren. Mithilfe einer etablierten analytischen Methode kann die Kristallisation metastabiler Silicaphasen identifiziert werden, deren Implikationen von der diagenetischen Modifizierung der Silizium-Isotopensignatur bis zur Einschätzung des Präservationspotentials fossilen Lebens auf dem Mars reicht. Die Ergebnisse der vorliegenden Arbeit führen zu neuen Konzepten für die Ordnungsprozesse eines der global bedeutendsten amorphen Geomaterialien. Diese evidenzbasierten Konzepte stehen in deutlichem Gegensatz zu der klassischen Theorie der gravitationsinduzierten Nanopartikelordnung, die in der Opalforschung seit 50 Jahren besteht.

As water is a unique liquid, so is amorphous silica a unique solid.

R. K. Iler, 1979

Chapter 1

Introduction

1.1 Amorphous silica - from solution to particles

Silicon dioxide is the most abundant chemical component of the Earth's crust. Chemical weathering of the Earth's crust is the ultimate source for the global silica cycle that links the geosphere, hydrosphere, and biosphere (Fig. 1.1). Additionally, weathering of silicate rocks by atmospherically derived carbon dioxide constitutes a critically important carbon sink; thus, aqueous alteration connects the global carbon and silica cycle (Gaillardet et al. 1999, Goudie & Viles 2012). Aqueous alteration of silicate minerals leads to the *in situ* formation of amorphous silica ($SiO_2 \cdot nH_2O$) at mineral surfaces (Hellmann et al. 2007, Olsson et al. 2012) or release of silicic acid into aqueous fluids, followed by amorphous nanoparticle precipitation through biogenic and abiogenic processes (Williams & Crerar 1985, Kröger et al. 1999, Marin-Carbonne et al. 2014). Globally, biogenic amorphous silica is dominantly precipitated as skeletal material of marine organisms such as diatoms, radiolaria, and siliceous sponges, and contributes significantly to the formation of chert in deep-sea sediments (DeMaster 1981, Maliva et al. 1989).

Abiogenic amorphous silica often consists of nanoparticle aggregates and occurs in many modern terrestrial environments in the form of desert varnish, hot-spring deposits, silcrete, and alteration products of volcanic rocks and deep-weathering environments (Darragh et al. 1966, Lynne et al. 2005, Perry et al. 2006, Thompson Stiegler et al. 2008, Liesegang & Milke 2014). Amorphous silica was also identified on the surface of Mars by orbiter- and rover-based spectroscopy and as a nanoparticulate alteration product in Martian meteorites (Milliken et al. 2008, Lee et al. 2016). The X-ray amorphous silica precipitates on Earth and Mars are referred to as opal-A (Jones & Segnit 1971).

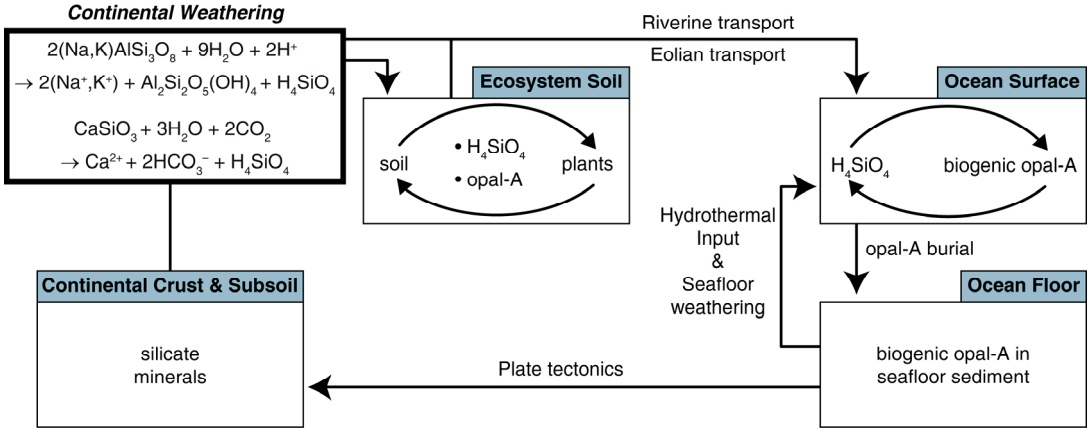

Figure 1.1. Schematic description of the global biogeochemical silica cycle since the Phanerozoic (modified after Struyf et al. 2009). The two left boxes represent the ultimate source for the global silica cycle: chemical weathering of the continental crust. Aqueous alteration of silicate minerals in the Earth´s crust and subsoil, e.g., alkali feldspar and wollastonite, liberates monosilicic acid (H_4SiO_4) into solution followed by local precipitation of amorphous silica (opal-A) in fractures, pores, and as pseudomorphs. Rivers transport monosilicic acid into the ocean. Opal-A is transported both as dust and in rivers. The two right boxes represent the oceanic silica pool. Significant amounts of biogenic opal-A are deposited on the seafloor and undergo diagenesis and subduction.

Australia - the largest continental silica archive

The Upper Cretaceous sedimentary rocks of the Great Artesian Basin (GAB) in Australia (Fig. 1.2) are an ideal archive - with a regional extent rarely found on Earth - for the formation and ordering processes of inorganically precipitated opal-A. Extensive amorphous silica precipitation records acidic oxidative weathering of sediments for the past ~90 Ma (Thiry et al. 2006, Rey 2013, Liesegang & Milke 2014), at temperatures below ~45 °C (Rondeau et al. 2004). From ~130 to ~93 Ma, the shallow epicontinental Eromanga Sea covered about 60% of Australia (Frakes et al. 1987, Rey 2013) and produced the major opal-bearing strata at the western extent of the GAB. During this period, deposition of terrestrial and marine clastic sediments in the poorly oxygenated marine to fluvial-deltaic environment resulted in the Aptian-Albian Bulldog Shale comprising pyrite and carbonaceous-rich mud- and siltstones interbedded with fine sandstones (Rey 2013). Deposition of the fluvial-lacustrine to coastal plain Winton Formation (97-93 Ma) marks the regression of the Eromanga Sea (Alexander et al. 2006, Rey 2013) and onset of prolonged erosion and chemical weathering of the GAB associated with extensive silicate dissolution and silica precipitation.

Most authors argue that at the opal fields of the GAB weathering of feldspar, mica, and clay minerals liberated silica into solution (Darragh et al. 1966, Senior et al. 1977, Barnes et al. 1992). These silica-laden solutions were trapped in cavities and along groundwater permeability barriers. Evaporation gradually supersaturated the trapped solutions, eventually leading to precipitation of amorphous silica and formation of opal-A in fractures and pores of the host rocks and during mineral replacement. Generally, the opals studied here were collected at four locations (Fig. 1.2) and originate from lithologies ~20–40 m below the present day surface. The amorphous precipitates at the opal fields Andamooka and Coober Pedy (Bulldog Shale), and Yowah (Winton Formation) are embedded in sub-horizontal sequences of kaolinized Cretaceous sedimentary rocks that grade from the surface down to unweathered parent rock (Senior et al. 1977, Carr et al. 1979, Barnes et al. 1992). The Mintabie opal field is exceptional because amorphous silica is primarily hosted by the fluviodeltaic Ordovician sand- and siltstones of the Mintabie beds (Barnes et al. 1992, Thiry et al. 2006) a few meters beneath the weathered and largely eroded Lower Cretaceous lithologies.

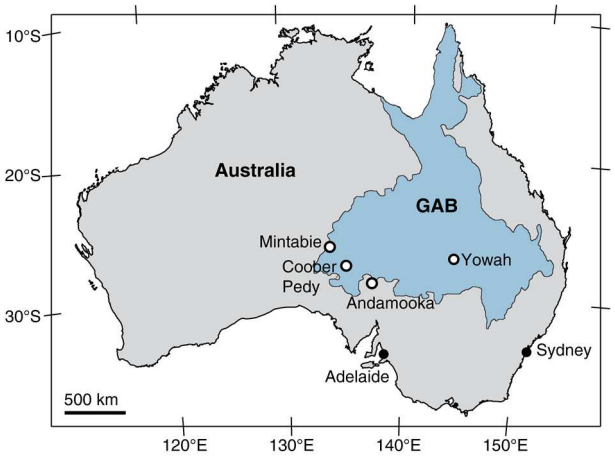

Figure 1.2. Location map of the samples studied here, with the outlined Great Artesian Basin (GAB) and the sample sites in South Australia (Andamooka, Coober Pedy, Mintabie) and Queensland (Yowah).

Silica polymerization and particle growth

A central problem in opal research is the complexity of the mostly unknown natural fluids they precipitate from. However, extensive experimental and modeling work on the silica system provides a conclusive fundament to approach amorphous silica nucleation and growth in sedimentary systems (Iler 1979, Rimstidt & Barnes 1980, Bogush & Zukoski 1991, Icopini et al. 2005). Silicate dissolution reactions liberate monomeric silicic acid (H_4SiO_4) into solution. At ambient conditions and sufficiently high supersaturation (~60–130 ppm SiO_2) these solutions become oversaturated with respect to amorphous silica (Iler 1979, Rimstidt & Barnes 1980, Williams et al. 1985, Gunnarsson & Arnórsson 2000). Although quartz is the thermodynamically stable silica phase at ambient conditions, metastable opal-A precipitates initially from such solutions, even if suitable solid crystal surfaces are available. It is unlikely that quartz co-precipitates with amorphous silica since quartz grows much slower (Iler 1979, Rimstidt & Barnes 1980, Worden et al. 2012). While a classical model satisfactorily describes quartz nucleation and growth as a silica monomer-by-monomer addition process, it often fails to explain amorphous silica nanoparticle growth and ordering processes in nature (Icopini et al. 2005, Liesegang & Milke 2014).

In solution, particle formation is initiated by condensation reactions, when the silanol groups (Si-OH) of hydrated silica tetrahedra form ≡Si-O-Si≡ bonds liberating H_2O (Fig. 1.3). Starting from oligomers, fractal polymers, ring structures, macromolecules, and primary sol particles form. These particles grow by addition of silica monomers and polymers on the surface or by aggregation with other particles (Bogush & Zukoski 1991; Icopini et al. 2005, Tobler et al. 2009). Dissociation of silanol (Si-OH → $Si\text{-}O^-$ + H^+) creates a negative particle surface charge at pH values above ~2–3. In electrolytes, counter-ions accumulate close to this negatively charged surface and form a diffuse electrical double-layer whose extent, the Debye screening length λ_D, is inversely proportional to the square root of the ionic strength (Israelachvili 2011). When particles approach, their double-layers overlap and repulse each other. With little or no charge repulsion, particle collision results in the formation of interparticle bonds. Electron microscopy shows that spheres in natural opal-A consist of subparticles tens of nanometers in size, indicating aggregation of metastable precursors as the major late-stage growth process (Darragh et al. 1966, Gaillou et al. 2008, Liesegang & Milke 2014).

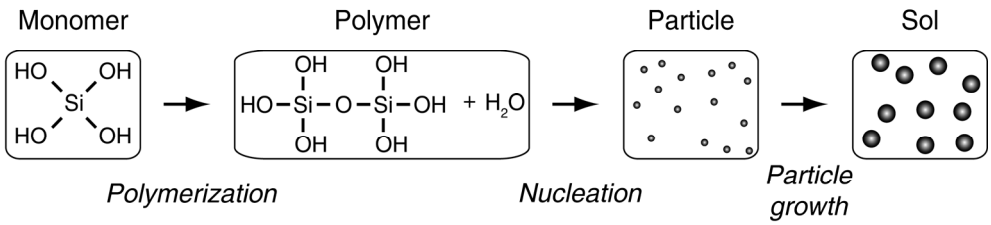

Figure 1.3. Schematic particle formation process in solutions supersaturated with respect to amorphous silica. Particle growth processes include Ostwald ripening, particle aggregation, and deposition of monomers and polymers on the respective particle surface. In a stable sol, particles exist as free units with repulsive interaction.

In the literature on natural amorphous silica some descriptive terms are used synonymously, despite their established definitions in colloid science. For the purpose of this thesis, the following terminology is used in accordance with Iler (1979) and the International Union of Pure and Applied Chemistry (IUPAC):

Monosilicic acid (or soluble silica): H_4SiO_4.

Colloidal silica: Polymerized species or particles dispersed in a fluid that have at least in one direction a dimension roughly between 1 nm and 1 µm.

Silica sol: Dispersions of colloidal silica particles in a liquid.

Silica gel: Rigid non-fluid colloidal or polymer network that is expanded throughout its whole volume by a fluid in pores of submicrometer dimensions.

1.2 The amorphous-to-crystalline pathway of silica nanoparticles

Amorphous silica nanoparticles are ubiquitous in the Earth's bio- and geosphere. However, information about abiogenic silica sphere formation, growth, and ordering processes in nature is limited (Conrad et al. 2007, Liesegang & Milke 2014). This knowledge gap is surprising, because synthetic silica spheres with distinct size, dispersity, and surface properties are extensively utilized for nanotechnological applications, such as surfactants, abrasives, and biomedical indicators (Tiarks et al. 2001, Ahn et al. 2004, Schönbächler et al. 2013). Jones et al. (1964) showed through electron micrographs that ordered lattices in natural opal-A consist of spheres of amorphous silica 150–350 nm in diameter. Novel high-resolution analytical methods show that metastable amorphous particles are an essential precursor for crystal formation and growth processes in natural systems, e.g., calcium carbonate, carbonated hydroxyapatite, and dolomite (Pouget et al. 2009, Mahamid et al. 2010, Rodriguez-Blanco et al. 2015). These nonclassical crystallization processes are classified as crystallization by particle attachment (CPA) (De Yoreo et al. 2015). Ostwald ripening, i.e., dissolution of small particles in favor of growing larger particles, likely proceeds concurrently (Lupulescu & Rimer 2014). Of the natural inorganic mineral systems developing via CPA, only amorphous silica has been reported to exhibit three-dimensional long-range ordering of isotropic nanoparticles. These ordered lattices are the natural prototype material for colloid-based 3D-ordered arrays used for applications such as microlasers, sensors, photonic crystals, and inverse opals (Shkunov et al. 2002, Waterhouse & Waterland 2007, Shin et al. 2010, Kim et al. 2011). Despite its abundance and prototype character, the processes driving the natural silica colloid system from the disordered toward an ordered state have still not been clarified.

To date, the formation and ordering of uniform silica spheres is commonly attributed to gravitational sphere settling at quiescent conditions in sealed environments (Darragh et al. 1966, Pewkliang et al. 2008, Rey 2013). Traditionally, a gelling process of polymers or colloidal dispersions is considered to precede silica sphere formation and ordering (Darragh et al. 1966, Pecover 2007, Gaillou et al. 2008, Pewkliang et al. 2008, Rey 2013). Previous studies agree that gravity and short-range particle interaction potentials alone

create structural order when uniform spheres grow inside this gel and settle from it. However, redispersion from a gel into a sol (gel-sol process) requires depolymerization of the gel network and subsequent neoformation of spherical particles. Experimental work lacks evidence for such a gel-to-sol transformation in the amorphous silica system. The alternative to the traditional view is sphere growth and ordering in a sol (Iler 1979, Liesegang & Milke 2014). This discrepancy illustrates the conflict between traditional views in opal research since the past 50 years, field evidence, and established concepts from silica synthesis and modeling.

Silica diagenesis

After deposition, amorphous silica undergoes diagenesis. The gradual transformation proceeds from metastable opal phases to quartz following the sequence opal-A → opal-CT → opal-C → quartz (Kastner et al. 1977, Mizutani 1977). The transformation rates are slow enough that metastable silica phases can persist. Mineralogical and textural changes dominantly occur by dissolution-precipitation reactions concurrent with a progressive decrease of tridymite stacking in favor of cristobalite stacking in opal-CT (Mizutani 1977, Rice et al. 1995). It is widely assumed that opal-CT, on land and in deep-sea sediments, forms by transformation from opal-A (Kastner et al. 1977, Hesse 1989, Lynne at al. 2005). Commonly, X-ray powder diffraction is used as a fingerprint method to trace the post-depositional history of marine sediments and siliceous sinter deposits (Mizutani 1977, Rice et al. 1995, Rodgers et al. 2004). However, X-ray diffraction is considered to be insensitive to the mineralogical maturation of opal-A, unless substantial micromorphological changes emerge (Lynne & Campbell 2004, Rodgers et al. 2004). Additionally, more sensitive analytical methods, i.e., Raman spectroscopy, have not provided a conclusive deconvolution of the opal-A spectrum into its separate peak components yet. Therefore, the early stage of diagenetic amorphous silica transformation remains to be explained.

1.3 Main chapters of the thesis

The following three chapters comprise an integrated effort to understand the processes that create structural order in natural amorphous silica. For this purpose, ordering is subdivided into two different categories: (1) three-dimensional order on the level of colloidal dimensions and (2) three-dimensional order on the level of atomic dimensions. Further, this thesis aims to clarify ordering processes in three different contexts: mineral replacement, fracture filling, and crystallization during early-stage diagenesis. Clarification of opal formation and ordering in these contexts requires high-resolution morphological, chemical, and structural analyses of opals and associated minerals combined with colloid-chemical models from materials science. In the following the different analytical techniques used during this thesis are summarized. A detailed description of the applied analytical methods is provided in the respective chapters.

To probe the nanoscale morphology of amorphous silica precipitates scanning electron microscopy (SEM) was used. Nanometer-sized structures in opal-A were investigated by preparing the samples by mild etching in a 10 vol% hydrofluoric acid solution and subsequent tungsten sputter-coating. This effectively improves the surface electrical conductivity and the image resolution necessary for the analysis of particles with a diameter typically below 40 nm. Using Focused ion beam - scanning electron microscopy (FIB-SEM) I was able to visualize the three-dimensional micro- and nanostructures of predefined sample volumes. With each step, tens of nanometers of the material were removed and the newly produced surface was imaged. Subsequently, processed images at a pixel resolution of 7 x 7 nm^2 were reassembled into a coherent 3D view of the studied material.

The chemical composition of the opals and their associated minerals was determined by electron probe microanalysis (EPMA) at a spatial resolution up to one micrometer. Thus, for all samples I obtained the chemical composition of the same material that was also characterized micromorphologically and crystallographically. EPMA provides significant advances over bulk analysis because it permits the geochemical characterization of inclusion-free sample areas.

X-ray diffraction and micro-Raman spectroscopy was used to identify the structural order of amorphous silica at the atomic scale. Contrary to conventionally used pulverized bulk samples, I applied non-destructive X-ray microdiffraction (μ-XRD^2) at a beam diameter of 50 μm. With each analysis an area of ~2000 $μm^2$ of material was probed that was previously characterized by EPMA and SEM. This approach allowed minimizing the interfering contribution of non-silica mineral phases that modify peak shapes and intensities of diffraction patterns. Micro-Raman spectroscopy complemented the high spatial resolution XRD analysis.

Chapter 2 (published in *Scientific Reports*, 2017)

This chapter provides a novel framework for the volume-preserving replacement of calcium carbonate by amorphous silica. In bivalve shells from Coober Pedy (South Australia), amorphous silica replaces twinned calcite crystals via an interface-coupled dissolution-precipitation reaction. Based on electron microscopy and nanotomography, I identify that continuous nanoparticle formation, growth, and ordering create photonic crystals several millimeters in size, while preserving calcite crystallographic orientations.

Moritz Liesegang and Ralf Milke designed the project and developed the final model. Moritz Liesegang conducted 3D reconstructions and interpretations of FIB-SEM data, and collected and interpreted SEM, X-ray microdiffraction, petrographic microscopy, and EPMA data and wrote the manuscript. Jürgen Ganzel supplied sample material. Christine Kranz and Gregor Neusser (Institute of Analytical and Bioanalytical Chemistry, Ulm University) guided FIB-SEM data acquisition.

Chapter 3 (published in *Minerals*, 2018)

This chapter presents the results of a multi-method investigation using petrographic microscopy, X-ray microdiffraction, micro-Raman spectroscopy, SEM, and EPMA of opal-A from the Andamooka and

Mintabie opal fields at South Australia. Electron microscopic observation indicates that colloid flow and post-depositional shearing create and destroy ordered sphere arrangements, even at the scale of centimeter-long specimens. The results also imply that an interface-coupled dissolution-precipitation process operates during dolomite-silica replacement, similar to the calcite-silica system.

Moritz Liesegang and Ralf Milke conceived and designed the study. Moritz Liesegang collected and analyzed all SEM, EPMA, petrographic microscopy, X-ray microdiffraction, and Raman spectroscopy data and wrote the manuscript. Both authors discussed the results and commented on the manuscript. Jürgen Ganzel supplied sample material.

Chapter 4 (published in *Sedimentary Geology*, 2018)

In this part of the thesis I focus on the post-depositional early-diagenetic maturation of amorphous silica. In the studied amorphous silica, opal-A transforms into opal-CT via nanoscale *in situ* nucleation and growth of low-tridymite/cristobalite domains. I use highly resolved, non-destructive X-ray microdiffraction to identify the early-stage opal-A crystallization. SEM and EPMA analysis, heating experiments, and diffraction pattern modelling complement the high-resolution analytical approach.

Moritz Liesegang and Ralf Milke conceived and designed the study. Moritz Liesegang collected and analyzed all SEM, X-ray microdiffraction, petrographic microscopy, and EPMA data and wrote the manuscript. Jürgen Ganzel provided sample material. Christoph Berthold (Eberhard Karls Universität Tübingen) provided access to X-ray microdiffraction facilities and helped in discussing the data and revising the manuscript.

1.4 References

Ahn, Y., Yoon, J.Y., Baek, C.W., and Kim, Y.K. (2004). Chemical mechanical polishing by colloidal silica-based slurry for micro-scratch reduction. Wear, 257, 785-789.

Alexander, E.M., Sansome, A., and Cotton, T.B. (2006). Lithostratigraphy and environments of deposition. In: T.B. Cotton, M.F. Scardigno und J.E. Hibburt, Hg. 2006. The petroleum geology of South Australia, Vol. 2: Eromanga Basin. 2nd edition. Department of Primary Industries and Resources. Petroleum Geology of South Australia Series.

Barnes, L.C., Townsend, I.J., Robertson, R.S., and Scott, D.C. (1992). Opal: South Australia's gemstone (Handbook No. 5); Department of Mines and Energy, Geological Survey of South Australia: Parkside, Australia.

Bogush, G.H. und Zukoski, C.F., 1991. Uniform silica particle precipitation: An aggregative growth model. Journal of Colloid and Interface Science, 142, 19-34.

Carr, S.G., Olliver, J.G., Conor, C.H.H., and Scott, D.C. (1979). Andamooka opal fields: The geology of the precious stones field and the results of the subsidised mining program. Report of Investigations 51, Department of Mines and Energy, Geological Survey of South Australia: Adelaide, Australia.

Conrad, C.F., Icopini, G.A., Yasuhara, H., Bandstra, J.Z., Brantley, S.L., and Heaney, P.J. (2007). Modeling the kinetics of silica nanocolloid formation and precipitation in geologically relevant aqueous solutions. Geochimica et Cosmochimica Acta, 71, 531-542.

Darragh, P., Gaskin, A., Terrell, B., and Sanders, J. (1966). Origin of precious opal. Nature, 209, 13-16.

DeMaster, D.J. (1981). The supply and accumulation of silica in the marine environment. Geochimica et Cosmochimica Acta, 45, 1715-1732.

De Yoreo, J.J., Gilbert, P.U.P.A., Sommerdijk, N.A.J.M., Penn, R.L., Whitelam, S., Joester, D., Zhang, H., Rimer, J.D., Navrotsky, A., Banfield, J.F., Wallace, A.F., Michel, F.M., Meldrom, F.C., Cölfen, H., and Dove, P.M. (2015). Crystallization by particle attachment in synthetic, biogenic, and geologic environments. Science, 349, aaa6760.

Frakes, L.A., Burger, D., Apthorpe, M., Wiseman, J., Dettmann, M., Alley, N., Flint, R., Gravestock, D., Ludbrook, N., Backhouse, J., Skwarko, S., Scheibnerova, V., McMinn, A., Moore, P.S., Bolton, B.R., Douglas, J.G., Christ, R., Wade, M., Molnar, R.E., McGowran, B., Balme, B.E., and Day, R.A. (1987). Australian Cretaceous shorelines, stage by stage. Palaeogeography, Palaeoclimatology, Palaeoecology, 59 , 31-48.

Gaillou, E., Fritsch, E., Aguilar-Reyes, B., Rondeau, B., Post, J., Barreau, A., and Ostroumov, M. (2008). Common gem opal: An investigation of micro- to nano-structure. American Mineralogist, 93, 1865-1873.

Gaillardet, J., Dupré, B., Louvat, P., and Allegre, C.J. (1999). Global silicate weathering and CO_2 consumption rates deduced from the chemistry of large rivers. Chemical Geology, 159, 3-30.

Goudie, A.S. and Viles, H.A. (2012). Weathering and the global carbon cycle: Geomorphological perspectives. Earth-Science Reviews, 113, 59-71.

Gunnarsson, I. and Arnórsson, S. (2000). Amorphous silica solubility and the thermodynamic properties of H_4SiO_4 in the range of 0 to 350°C at P_{sat}. Geochimica et Cosmochimica Acta, 64, 2295-2307.

Hellmann, R., Wirth, R., Daval, D., Barnes, J.-P., Penisson, J.-M., Tisserand, D., Epicier, T., Florin, B., and Hervig, R.L. (2012). Unifying natural and laboratory chemical weathering with interfacial dissolution-reprecipitation: A study based on the nanometer-scale chemistry of fluid–silicate interfaces. Chemical Geology, 294-295, 203-216.

Israelachvili, J.N. (2011). Intermolecular and Surface Forces. 3rd edition. Boston: Academic Press.

Jones, J.B. and Segnit, E.R. (1971). The nature of opal I. Nomenclature and constituent phases. Journal of the Geological Society of Australia, 18, 37-41.

Kastner, M., Keene, J.B., and Gieskes, J.M. (1977). Diagenesis of siliceous oozes - I. Chemical controls on the rate of opal-A to opal-CT transformation - an experimental study. Geochimica et Cosmochimica Acta, 41, 1041-1059.

Kim, S.H., Lee, S.Y., Yang, S.M., and Yi, G.R. (2011). Self-assembled colloidal structures for photonics. NPG Asia Materials, 3, 25-33.

Kröger, N., Deutzmann, R., and Sumper, M. (1999). Polycationic peptides from diatom biosilica that direct silica nanosphere formation. Science, 286, 1129-1132.

Liesegang, M. and Milke, R. (2014). Australian sedimentary opal-A and its associated minerals: Implications for natural silica sphere formation. American Mineralogist, 99, 1488-1499.

Lee, M.R., MacLaren, I., Andersson, S.M.L., Kovacs, A., Tomkinson, T., Mark, D.F., and Smith, C.L. (2015). Opal-A in the Nakhla meteorite: A tracer of ephemeral liquid water in the Amazonian crust of Mars. Meteoritics & Planetary Science, 50, 1362-1377.

Lupulescu, A.I. and Rimer, J.D. (2014). In situ imaging of silicalite-1 surface growth reveals the mechanism of crystallization. Science, 344, 729-732.

Lynne, B.Y. and Campbell, K.A. (2004). Morphologic and mineralogic transitions from opal A to opal-CT in low-temperature siliceous sinter diagenesis, Taupo Volcanic Zone, New Zealand. Journal of Sedimentary Research, 74, 561-579.

Lynne, B., Campbell, K., Moore, J., and Browne, P. (2005). Diagenesis of 1900-year-old siliceous sinter (opal-A to quartz) at Opal Mound, Roosevelt Hot Springs, Utah, U.S.A. Sedimentary Geology, 179, 249-278.

Mahamid, J., Aichmayer, B., Shimoni, E., Ziblat, R., Li, C., Siegel, S., Paris, O., Fratzl, P., Weiner, S., Addadi, L., and Tirrell, D.A. (2010). Mapping amorphous calcium phosphate transformation into crystalline mineral from the cell to the bone in zebrafish fin rays. Proceedings of the National Academy of Sciences, 107, 6316-6321.

Maliva, R., Knoll, A., and Siever, R. (1989). Secular change in chert distribution: a reflection of evolving biological participation in the silica cycle. Palaios, 4, 519–532.

Marin-Carbonne, J., Robert, F., and Chaussidon, M. (2014). The silicon and oxygen isotope compositions of Precambrian cherts: A record of oceanic paleo-temperatures? Precambrian Research, 247, 223-234.

Milliken, R.E., Swayze, G.A., Arvidson, R.E., Bishop, J.L., Clark, R.N., Ehlmann, B.L., Green, R.O., Grotzinger, J.P., Morris, R.V., Murchie, S.L., Mustard, J.F., and Weitz, C. (2008). Opaline silica in young deposits on Mars. Geology, 36, 847-850.

Mizutani, S. (1977). Progressive ordering of cristobalitic silica in the early stage of diagenesis. Contributions to Mineralogy and Petrology, 61, 129-140.

Morey, G.W., Fournier, R.O., & Rowe, J.J. (1964). The solubility of amorphous silica at 25°C. Journal of Geophysical Research, 69, 1995-2002.

Olsson, J., Bovet, N., Makovicky, E., Bechgaard, K., Balogh, Z., and Stipp, S.L.S. (2012). Olivine reactivity with CO_2 and H_2O on a microscale: implications for carbon sequestration. Geochimica et Cosmochimica Acta, 77, 86-97.

Pecover, S.R. (2007). Australian Opal Resources: Outback Spectral Fire. Rocks & Minerals, 82, 102-115.

Perry, R.S., Lynne, B.Y., Sephton, M.A., Kolb, V.M., Perry, C.C., and Staley, J.T. (2006). Baking black opal in the desert sun: The importance of silica in desert varnish. Geology, 34, 537-540.

Pewkliang, B., Pring, A., and Brugger, J. (2008). The formation of precious opal: Clues from the opalisation of bone. Canadian Mineralogist, 46, 139-149.

Pouget, E.M., Bomans, P.H.H., Goos, J.A.C.M., Frederik, P.M., de With, G., and Sommerdijk, N.A.J.M. (2009). The initial stages of template-controlled CaCO3 formation revealed by cryo-TEM. Science, 323, 1455-1458

Rey, P.F. (2013). Opalisation of the Great Artesian Basin (central Australia): an Australian story with a Martian twist. Australian Journal of Earth Sciences, 60, 291-314.

Rice, S.B., Freund, H., Huang, W.L., Clouse, J.A., and Isaacs, C.M. (1995). Application of Fourier transform infrared spectroscopy to silica diagenesis: the opal-A to opal-CT transformation. Journal of Sedimentary Research, 65, 639-647.

Rodgers, K.A., Browne, P.R.L., Buddle, T.F., Cook, K.L., Greatrex, R.A., Hampton, W.A., Herdianita, N.R., Holland, G.R., Lynne, B.Y., Martin, R., Newton, Z., Pastars, D., Sannazarro, K.L., and Teece, C.I.A. (2004). Silica phases in sinters and residues from geothermal fields of New Zealand. Earth-Science Reviews, 66, 1–61.

Rodriguez-Blanco, J.D., Shaw, S., and Benning, L.G. (2015). A route for the direct crystallization of dolomite. American Mineralogist, 100, 1172-1181.

Rondeau, B., Fritsch, E., Guiraud, M., and Renac, C. (2004). Opals from Slovakia („Hungarian" opals): a re-assessment of the conditions of formation. European Journal of Mineralogy, 16, 789-799.

Schönbächler, A., Glaied, O., Huwyler, J., Frenz, M., and Pieles, U. (2013). Indocyanine green loaded biocompatible nanoparticles: Stabilization of indocyanine green (ICG) using biocompatible silica-poly (ε-caprolactone) grafted nanocomposites. Journal of Photochemistry and Photobiology A: Chemistry, 261, 12-19.

Senior, B.R., McColl, D.H., Long, B.E., and Whiteley, R.J. (1977). The geology and magnetic characteristics of precious opal deposits, southwest Queensland. BMR Journal of Australian Geology and Geophysics, 2, 241-251.

Shin, J., Braun, P. V., & Lee, W. (2010). Fast response photonic crystal pH sensor based on templated photopolymerized hydrogel inverse opal. Sensors and Actuators B: Chemical, 150, 183-190.

Shkunov, M.N., Vardeny, Z.V., DeLong, M.C., Polson, R.C., Zakhidov, A.A., and Baughman, R.H. (2002). Tunable, gap-state lasing in switchable directions for opal photonic crystals. Advanced Functional Materials, 12, 21-26.

Thompson Stiegler, M., Lowe, D., and Byerly, G. (2008). Abundant pyroclastic komatiitic volcanism in the 3.5-3.2 Ga Barberton greenstone belt, South Africa. Geology, 36, 779-782.

Thiry, M., Milnes, A.R., Rayot, V., and Simon-Coinçon, S. (2006). Interpretation of palaeoweathering features and successive silicifications in the Tertiary regolith of Inland Australia. Journal of the Geological Society, 163, 723-736.

Tiarks, F., Landfester, K., and Antonietti, M. (2001). Silica nanoparticles as surfactants and fillers for latexes made by miniemulsion polymerization. Langmuir, 17, 5775-5780.

Waterhouse, G.I. and Waterland, M.R. (2007). Opal and inverse opal photonic crystals: fabrication and characterization. Polyhedron, 26, 356-368.

Worden, R.H., French, M.W., and Mariani, E. (2012). Amorphous silica nanofilms result in growth of misoriented microcrystalline quartz cement maintaining porosity in deeply buried sandstones. Geology, 40, 179-182.

Chapter 2

Silica nanoparticle aggregation in calcite replacement reactions

Published as:

Liesegang, M., Milke, R., Kranz, C., and Neusser, G. (2017). Silica nanoparticle aggregation in calcite replacement reactions. *Scientific Reports*, 7, 14550.

https://doi.org/10.1038/s41598-017-06458-8

2.1 Abstract

Natural nanoparticles are fundamental building blocks of Earth's bio- and geosphere. Amorphous silica nanoparticles are ubiquitous in nature, but fundamental knowledge of their interaction mechanisms and role in mineral replacement reactions is limited. Here we show how silica nanoparticles replace Cretaceous calcite bivalve shells in a volume- and texture-preserving process. Electron tomography reveals that mineral replacement transfers calcite crystallographic orientations to twinned photonic crystals composed of face-centered cubic silica sphere stacks. During the face-specific replacement process, silica nanoparticles continuously nucleate, aggregate, and form a lattice of uniform spheres parallel to calcite low-energy facets. We explain the replacement process with a new model that unifies recently proposed, probably universal mechanisms of interface-coupled dissolution-precipitation and aggregation-based crystallization; both key mechanisms in geological processes and nanomaterials design and synthesis.

2.2 Introduction

In a first approximation, the Earth's crust consists of silicate rocks. Chemical weathering reactions of these rocks lead to the *in situ* formation of amorphous silica at silicate mineral surfaces (Hellmann et al. 2007) or release of silica into aqueous fluids, followed by amorphous nanoparticle precipitation through organic and inorganic processes (Williams & Crerar 1985, Kröger et al. 1999, Conrad et al. 2007, Marin-Carbonne et al. 2014). In recent years, amorphous nanoparticles have increasingly been identified as fundamental precursors for crystal formation and growth processes in natural systems (Pouget et al. 2009, Mahamid et al. 2010). These processes are classified as crystallization by particle attachment (CPA) (De Yoreo et al. 2015). However, despite its ubiquitous nature and prototype character for synthetic colloidal crystals (Miguez et al. 1997), fundamental knowledge of silica nanoparticle formation and ordering processes in nature is limited (Conrad et al. 2007, Liesegang & Milke 2014). This knowledge gap also includes the globally widespread interaction of calcium carbonate minerals with amorphous silica (Schmitt & Boyd 1981, Maliva & Siever 1988, Klein & Walter 1995). Our analytical results and schematic model fill this gap and show that calcite dissolution and silica precipitation are linked by a fluid-mediated replacement process that transfers atomic crystallographic information to an amorphous, mesoscale-ordered material in a natural weathering environment.

2.3 Materials and methods

Four bivalve shell samples with their respective host rock were collected in the Allan Rise precious opal field (WGS84 -29.3974°N 134.8581°E) located 52 km south of the Coober Pedy Township (South Australia). The samples were extracted from bulldozer cuts approximately 20 m below the present day surface. Shell samples analyzed are white to milky with moderate play-of-color (POC). Bivalve shells and their friable porous host rock (Supplementary Fig. 2.1) were cut using a diamond-impregnated steel lapidary saw cooled with water-free fluid.

Diamond polished thin sections (30 µm thick) were prepared using standard procedures. For polarized light microscopy, a Zeiss Axio Lab.A1 petrographic microscope was used. At least 400 intersection angles between straight twin and cleavage planes of crystals were measured and averaged over each sample. Non-destructive µ-XRD was used on thick sections, at the University of Tübingen (Germany), with a modified Bruker AXS micro-X-ray diffractometer D8 Discover with focusing X-ray optics and a VÅNTEC500 2D-detector. Diffractograms (Supplementary Fig. 2.2) were recorded for 300 s at a beam diameter of 50 µm in the 2θ range 7–67°, using Co-Kα radiation at 30 kV and a tube current of 30 mA. Quantitative element concentrations (Supplementary Table 1) were determined on carbon-coated, polished thin sections, using a JEOL JXA 8200 Superprobe operated at 15 kV acceleration voltage, 20 nA beam current, and a beam diameter of 10 µm. For each specimen, at least 30 crystals with 30 point analyses each were measured. The samples were analyzed for the elements Si, Ti, Al, Fe, Mg, Mn, Ca, Ba, Sr, Na, K, S, and P. Acquisition time for Na analysis was 5 s on peak and 5 s on background. Peak and background of other elements were measured for 10 s each. The instrument was internally calibrated using natural silicate, oxide, and basalt (VG-2) and rhyolite (VG-568) glass.

The morphologies of silica spheres and their subparticles were investigated on surfaces of thin sections and freshly fractured material by SEM. Specimens were etched in 10 vol % HF solution for 15 s, dried, and sputter-coated with ~15 nm W. Secondary electron images were obtained with a Zeiss Supra 40 VP Ultra SEM instrument, at an acceleration voltage 5 kV and beam current of 10 nA. Subparticles were identified with the InLens detection mode. For each specimen, sphere and subparticle diameters have been determined by averaging over at least 1000 manually measured particles. The sphere diameter dispersity has been calculated as relative standard deviation.

The sphere stack geometry of adjacent twin lamellae was characterized by FIB-SEM nanotomography of three pre-selected regions on thin sections. The thin sections were carbon-coated (~5 nm) to enhance electrical conductivity and mounted onto a SEM specimen stub. The sample sides were covered with silver glue to improve charge conduction between the top surface and the stub. Focused ion beam (FIB)-SEM nanotomography was conducted with a FEI Helios Nanolab 600 scanning electron microscope equipped with a focused Gallium-ion beam. To protect the sample from beam damage during FIB-milling, the surface was covered twice with a platinum layer using ion beam-induced deposition. A block face was generated by milling a regular cross section perpendicular to the twin plane of adjacent lamellae. After a cleaning cross section the area for the slice and view process was defined. Slice and view was performed using the software Auto Slice & View (FEI). Ion beam milling was conducted at 30 kV with a beam current of 93 pA. Secondary electron images were obtained at an acceleration voltage of 5 kV and beam current of 86 pA. The total number of slices ranged between 140 and 200 per sampled region. With each step, 20 nm of the material was removed and the newly produced surface was imaged with the SEM using the secondary electron signal recorded with the through lens detector. The pixel dimensions of a recorded image were set to 7×7 nm^2 (voxel size of $7 \times 7 \times 20$ nm^3).

Secondary electron images have been processed with the open source software Fiji (Schindelin et al. 2012). We used the SIFT plugin (Lowe 2004) for automatic alignment of the slice stacks. The aligned stacks were cropped and processed to reduce image noise using a fast Fourier transform filter. Subsequently, a manual grey level thresholding was applied to each image to segment the pore space from the data. Prior to image binarization, this image correction procedure minimized the interfering effects of scan distortions and electron charging during image acquisition. Segmented image stacks were directly volume-rendered by the Voxel function in Avizo 7.0, as shown in Supplemental Figure S2.3 and Video S2. The hexagonal close-packed lattice planes (Fig. 2.3) and the twin planes have been determined manually. Due to the possibility of bias in human judgement, we averaged 25 independent manual runs. We calculated the intersection angles between indexed planes from the normal vectors given by the Avizo software and measured them manually in suitable orientations (e.g., uvw [01-1], as shown in Supplemental Fig. 2.3) for comparison. The fcc lattice was confirmed measuring and calculating the angles between indexed planes, for example, (100) ∧ (111) = 55° and (110) ∧ (111) = 35°.

2.4 Results and discussion

Photonic crystals retain calcite crystallography

To demonstrate silica nanoparticle interaction and ordering processes, we use silica-replaced bivalve shells collected at Coober Pedy (South Australia) from unsilicified Early Cretaceous Bulldog Shale – a deeply chemically weathered, kaolinitic, marine siltstone (Supplementary Fig. 2.1). Transmitted light microscopy reveals that the investigated shells consist of a mosaic of anhedral, randomly oriented, optical photonic crystals up to 2.5 mm in size. Microdiffraction data confirm the X-ray amorphous nature of the studied material (Supplementary Fig. 2.2). The colors of the crystals cover the visible spectrum and upon rotation on the microscope stage, both color and intensity change. Figure 2.1 shows that observation between crossed polarizers reveals parallel striations (3–32 µm wide) that mimic polysynthetic twin lamellae on trigonal {018} indicative of recrystallized calcite ($CaCO_3$).

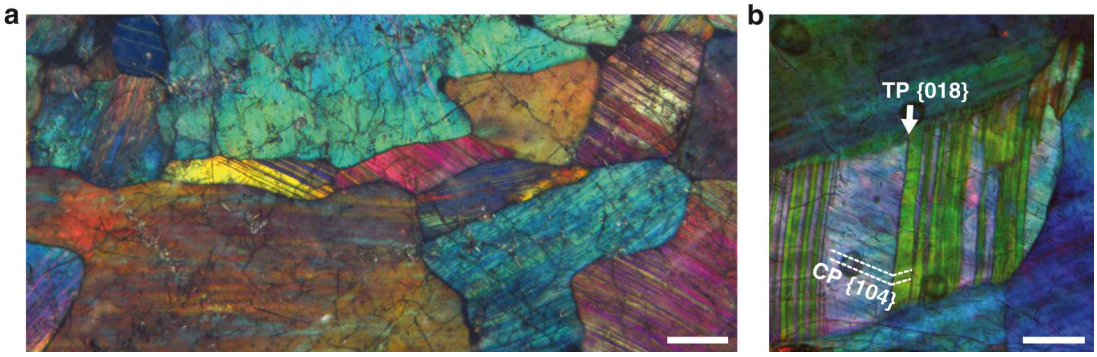

Figure 2.1. Microphotographs of silica photonic crystals between crossed polarizers. (**a**) Striated photonic crystals with different colors and orientations. (**b**) Crystals display lamellae with periodically alternating colors. Twin (TP) and cleavage (CP) planes are consistent with calcite crystallographic orientations. Scale bars are 100 µm.

The twinned condition of the lamellae is visible as a periodic color variation in an A-B-A-B pattern. Within some lamellae, thin straight lines intersect with twin planes at an angle of 71.2 ± 1.5° (Fig. 2.1b). This angle compares closely with the angle between co-zonar calcite {104} cleavage and {018} twin planes at 70.75° (Turner et al. 1954); thus, it evidences that the replacement reaction is intimately coupled to calcite crystallographic orientations. The color variations of the photonic crystals arise from Bragg diffraction effects from colloidal arrays, visualized directly by scanning electron microscopy (SEM), showing that the crystals consist of coherently ordered silica spheres and air-filled pores (Fig. 2.2a). The sphere arrays perfectly replicate the twin lamellae of calcite in periodically changing orientations. The average sphere diameter varies between samples from 270–400 nm (size dispersion <3.5 %). Mild hydrofluoric acid etching of the spheres reveals internal core-shell structures with up to three concentric layers (Fig. 2.2b). These structures consist of spherical particles 30 ± 2 nm in diameter, which indicates that, at least in the final stage, particle aggregation is the major sphere growth mechanism.

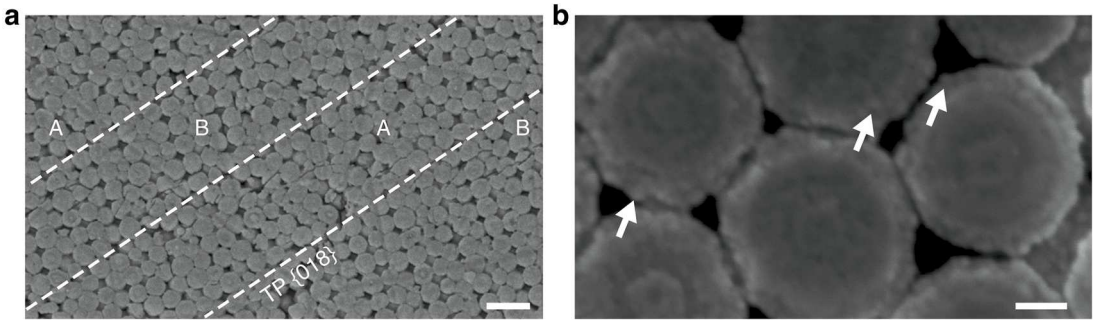

Figure 2.2. Secondary electron images of amorphous silica sphere geometry and microstructures. (**a**) Polished surface of a twinned crystal with alternating sphere array orientation in an A-B-A-B pattern. Dashed lines highlight the {018} twin planes (TP). (**b**) HF acid-etched spheres show a concentric layering. Arrows highlight ~30 nm-sized subparticles. Scale bars: (a) 1 µm, (b) 100 nm.

To evaluate how effectively the templating process captured the crystallographic elements of the calcite precursor, we analyzed the three-dimensional (3D) silica sphere packing and orientation in twin lamellae using focused ion beam (FIB)-SEM nanotomography at a voxel size of 7 × 7 × 20 nm^3. Figure 2.3a shows a tomographic image reconstruction of the pore space in adjacent twin lamellae. The uniform pore arrangement indicates uniform sphere arrays. The 3D reconstruction reveals that the lamellae consist of a close-packed lattice of spheres compatible with the face-centered cubic (fcc) structure. Twin and cleavage planes consist of a submicrometer layer of dislocated spheres. These geometric incompatibilities can arise along twin planes by converging sphere stacks and at cleavage planes by stacking faults introduced during growth. To identify the relationship between lattice planes of calcite and silica sphere arrays, we calculated the angles between the calcite {018} twin plane and indexed fcc {hkl} planes by vector analysis. We found that within successive lamellae fcc (111) planes form a zig-zag pattern with an angle of 70.1 ± 1.5° to the twin planes. This intersection angle reproduces the rational relation of {018} twin and {104} cleavage planes in calcite and confirms that calcite crystallographic planes template the fcc stacking sequence according to the relationship $\{104\}_{calcite}//(111)_{fcc}$. For preservation in the colloidal crystal, the calcite {104} lattice planes

must be thermodynamically most stable and dissolve the slowest. Both theoretical and experimental work (Titiloye et al. 1993, Didymus et al. 1993) support this basic principle, which under-lines the importance of anisotropic dissolution rates (Godinho et al. 2012) to extrapolate laboratory-based results to natural systems.

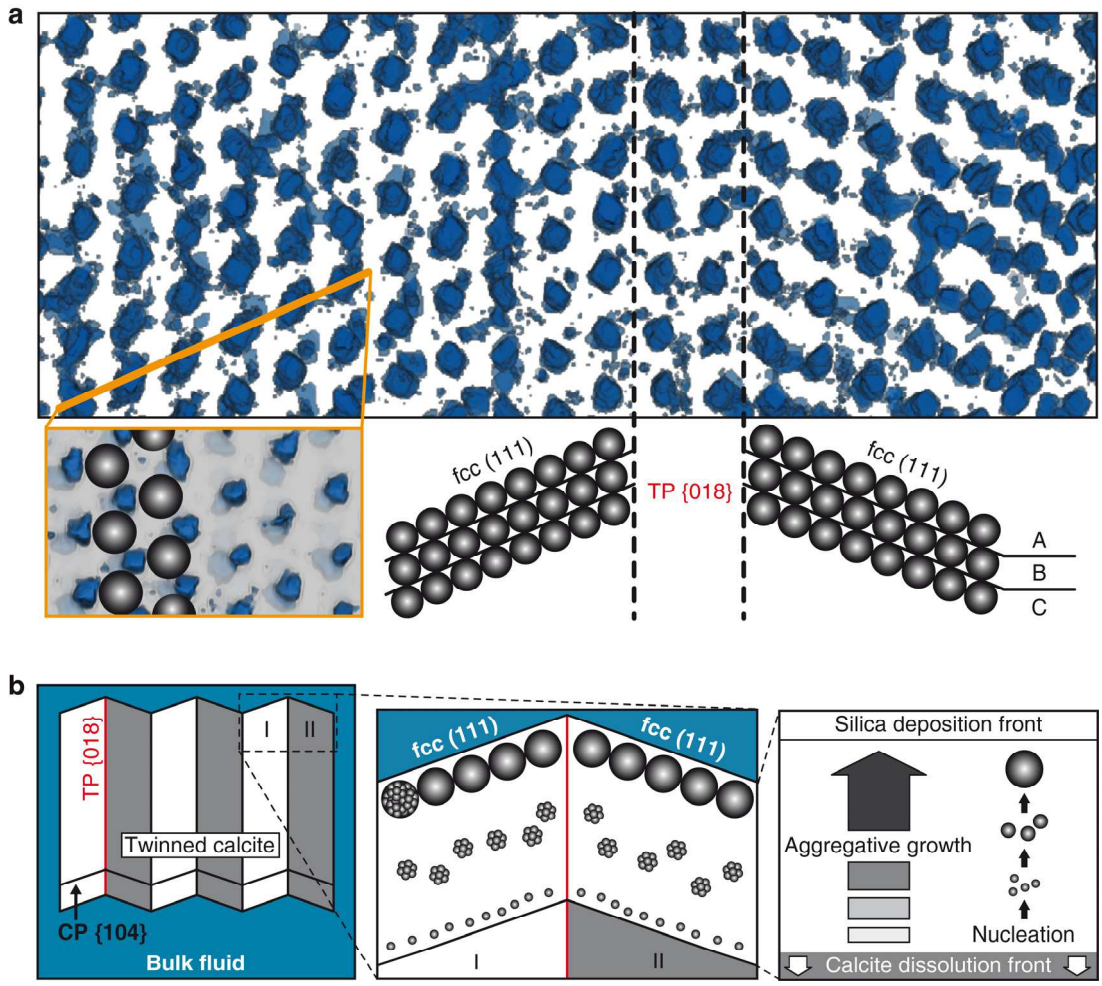

Figure 2.3. Nanoscale structures and schematic replacement process of twinned calcite crystals. **(a)** Three-dimensional visualization of pores in adjacent twin lamellae (4183 × 1733 nm^2), projected along uvw [01-1]. The calcite {018} twin plane (TP) separates A B C A B C ··· sphere stacking sequences of fcc lattices. The top view (lower left) shows spheres in the fcc (111) layer (1654 × 1043 nm^2). **(b)** The orientation of calcite {104} cleavage planes (CP) changes rhythmically between twins I and II. Amorphous silica particles nucleate close to the calcite surface, aggregate in the interfacial fluid film, and self-assemble into close-packed fcc (111) planes.

The nanoparticle-based replacement process

We combine our results into a generalized model that describes the pseudomorphic replacement of an atomic crystal by the orders of magnitude larger nanoparticle architecture, via a crystallization by particle attachment process (Fig. 2.3b). To date, abiogenic carbonate-silica replacement has been attributed to infilling of cavities created by bulk dissolution (Schmitt & Boyd 1981) or silicification controlled by the force of crystallization (Maliva & Siever 1988). Both concepts are inconsistent with the studied material due to (i) the preservation of crystallographic orientation and (ii) the amorphous and nanoporous nature of the

replacement silica. In fact, our observations point to a coupled dissolution-precipitation mechanism along a moving reaction interface (Putnis & Putnis 2007), controlled by fluid chemistry between the calcite dissolution front, $\{104\}_{calcite}$, and the silica sphere deposition front, $(111)_{fcc}$.

The highly selective nature of the replacement reaction indicates that calcite dissolution initiates silica precipitation. The dissolution reaction releases Ca^{2+} and CO_3^{2-} into the fluid film and creates a sharp localized pH and salinity rise (Molins et al. 2014) that gradually decreases toward the bulk fluid. This local change lowers the amorphous silica solubility, induces supersaturation and precipitation (Iler 1979, Marshall & Warakomski 1980), and confines particle nucleation close to the moving calcite dissolution front. In contrast to the classical LaMer nucleation-and-growth (LaMer & Dinegar 1950) and Ostwald ripening mechanisms (Marqusee & Ross 1983), particle growth in the natural precipitating system is not temporarily limited by the silica monomer concentration and does not compete with nucleation. Thus, particles grow homogeneously along a multistep aggregative pathway of increasingly large units at increasing distance from the calcite surface, in a process analogous to the formation of uniform silica nanocolloids from alkoxysilanes (Carcouët et al. 2014) and hydrothermal brine solutions (Conrad et al. 2007).

The uniformity of the sphere arrays described herein requires constant physicochemical conditions in the fluid film (e.g., ionic strength, pH, and nucleation/growth rate) throughout the entire replacement process. The nanoporous sphere fcc geometry (~26 % porosity) is permissive and enables mass transport and the necessary permanent fluid access to the calcite dissolution front. As soon as the calcite dissolution and silica deposition fronts advance synchronously, a steady state is established and small particles form continuously until the replacement process is completed. Once these particles move due to their Brownian motion, the competition between van der Waals attraction and electrostatic repulsion drives their interaction potential. The ions in the interfacial fluid film can neutralize the particle surface charge, compress the repulsive electrical double-layer, and promote the irreversible aggregation of marginally unstable particles (Iler 1979). Electron probe microanalyses show that up to 1.72 wt % of the fluid cations (primarily Al^{3+}, Supplementary Table 2.1), apart from silica, are structurally incorporated during particle growth (Liesegang & Milke 2014). The particles in the propagating fluid film continuously collide, stick together, and form larger more stable aggregates. The last active growth step is the aggregation of the observed ~30 nm-sized subparticles that form distinctly larger spheres with a narrow size distribution. The final spheres then self-assemble into minimum energy hexagonal close-packed fcc (111) planes that stack layer-by-layer parallel to the {104} lattice plane of calcite. Ultimately, the colloid undergoes a phase transition into the long-range ordered, thermodynamically favored fcc lattice (Miguez et al. 1997) that forms the bulk photonic crystal.

Implications for fluid-mediated replacement reactions

The model proposed herein offers a crystallization by particle attachment process that potentially operates over a wide range of replacement reactions by initially nanocolloidal amorphous and crystalline phases. These replacement reactions include, for example, silica and carbonate pseudomorphism and fossilization (Maliva & Siever 1988, Grotzinger & James 2000), or other replacement reactions crucial for palaeoenvironmental isotopic and redox condition studies such as chert nodule (Marin-Carbonne 2014) and pyrite (FeS_2) formation (Gabott et al. 2004). The oriented attachment of crystalline nanoparticles (De Yoreo et al. 2015) can be incorporated into our model and explains the transfer of crystallographic information (epitaxy) across the fluid film in interface-coupled dissolution-precipitation reactions. In addition, our results suggest a potential atomic crystal templating approach for the controllable synthesis of 3D self-assembled functional materials with ordered lattices and a single domain size of several millimeters. In the light of constant progress in high-resolution analytical instrumentation (De Yoreo & Sommerdijk 2016) and ever-increasing evidence of nanoparticles as fundamental building blocks in natural environments (De Yoreo et al. 2015), we propose that nanoparticle-based mineral formation is a key mechanism in fluid-mediated replacement reactions in geological processes and the synthesis of advanced functional materials, such as molecular sieves, heterogeneous catalysts, semiconductors, and photonic devices (Reboul et al. 2012, Brugger et al. 2010).

2.5 Acknowledgments

Funding for this research was provided by the German Research Council (DFG), grant number MI1205/5–1. We thank Jürgen Ganzel for supplying the samples. Christoph Berthold (Eberhard Karls Universität Tübingen) provided access to μ-X-ray facilities. We acknowledge support by the Open Access Publication Fund of the Freie Universität Berlin.

2.6 References

Brugger, J., Mcfadden, A., Lenehan, C.E., Etschmann, B., Xia, F., Zhao, J., and Pring, A. (2010). A novel route for the synthesis of mesoporous and low-thermal stability materials by coupled dissolution-reprecipitation reactions: mimicking hydrothermal mineral formation. Chimia 64, 693-698.

Carcouët, C.C.M.C., van de Put, M.W.P., Mezari, B., Magusin, P.C.M.M., Laven, J., Bomans, P.H.H., Friedrich, H., Esteves, A.C.C., Sommerdijk, N.A.J.M., van Benthem, R.A.T.M., and de With, G. (2014). Nucleation and growth of monodisperse silica nanoparticles. Nano Letters, 14, 1433-1438.

Conrad, C.F., Icopini, G.A., Yasuhara, H., Bandstra, J.Z., Brantley, S.L., and Heaney, P.J. (2007). Modeling the kinetics of silica nanocolloid formation and precipitation in geologically relevant aqueous solutions. Geochimica et Cosmochimica Acta, 71, 531-542.

De Yoreo, J.J. and Sommerdijk, N.A.J.M. (2016). Investigating materials formation with liquid-phase and cryogenic TEM. Nature Reviews Materials, 1, 16035.

De Yoreo, J.J., Gilbert, P.U.P.A., Sommerdijk, N.A.J.M., Penn, R.L., Whitelam, S., Joester, D., Zhang, H., Rimer, J.D., Navrotsky, A., Banfield, J.F., Wallace, A.F., Michel, F.M., Meldrom, F.C., Cölfen, H., and Dove, P.M. (2015). Crystallization by particle attachment in synthetic, biogenic, and geologic environments. Science, 349, pp. aaa6760.

Didymus, J.M., Oliver, P., Mann, S., DeVries, A.L., Hauschka, P.V, and Westbroek, P. (1993). Influence of low-molecular-weight and macromolecular organic additives on the morphology of calcium carbonate. Journal of the Chemical Society, Faraday Transactions, 89, 2891-2900.

Gabbott, S.E., Xian-Guang, X., Norry, M.J., and Siveter, D.J. (2004). Preservation of Early Cambrian animals of the Chengjiang biota. Geology, 32, 901-904.

Godinho, J. R., Piazolo, S., and Evins, L. Z. (2012). Effect of surface orientation on dissolution rates and topography of CaF_2. Geochimica et Cosmochimica Acta, 86, 392-403.

Grotzinger, J.P. and James, N.P. in Carbonate Sedimentation and Diagenesis in the Evolving Precambrian World (eds. Grotzinger, J.P. and James, N.P) 3-20 (Society for Sedimentary Geology, 2000).

Hellmann, R., Wirth, R., Daval, D., Barnes, J-P, Penisson, J.-M., Tisserand, D., Epicier, T., Florin, B., and Hervig, R.L. (2012). Unifying natural and laboratory chemical weathering with interfacial dissolution-reprecipitation: a study based on the nanometer-scale chemistry of fluid-silicate interfaces. Chemical Geology, 294, 203-216.

Iler, R.K. (1979). The Chemistry of Silica: Solubility, polymerization, colloid and surface properties, and biochemistry; Wiley: New York, USA.

Jones, J.B. and Segnit, E.R. (1971). The nature of opal I. Nomenclature and constituent phases. Journal of the Geological Society of Australia, 18, 37-41.

Klein, R.T. and Walter, L.M. (1995). Interactions between dissolved silica and carbonate minerals: An experimental study at 25-50°C. Chemical Geology, 125, 29-43.

Kröger, N., Deutzmann, R., and Sumper, M. (1999). Polycationic peptides from diatom biosilica that direct silica nanosphere formation. Science, 286, 1129-1132.

LaMer, V.K. and Dinegar, R.H. (1950). Theory, production and mechanism of formation of monodispersed hydrosols. Journal of the American Chemical Society, 72, 4847-4854.

Liesegang, M. and Milke, R. (2014). Australian sedimentary opal-A and its associated minerals: Implications for natural silica sphere formation. American Mineralogist, 99, 1488-1499.

Lowe, D.G. (2004). Distinctive image features from scale-invariant keypoints. International Journal of Computer Vision, 60, 91-110.

Mahamid, J., Aichmayer, B., Shimoni, E., Ziblat, R., Li, C., Siegel, S., Paris, O., Fratzl, P., Weiner, S., Addadi, L., and Tirrell, D.A. (2010). Mapping amorphous calcium phosphate transformation into crystalline mineral from the cell to the bone in zebrafish fin rays. Proceedings of the National Academy of Sciences, 107, 6316-6321.

Maliva, R.G. and Siever, R. (1988). Diagenetic replacement controlled by force of crystallization. Geology, 16, 688-691.

Marin-Carbonne, J., Robert, F., and Chaussidon, M. (2014). The silicon and oxygen isotope compositions of Precambrian cherts: A record of oceanic paleo-temperatures? Precambrian Research, 247, 223-234.

Marqusee, J.A. and Ross, J. (1983). Kinetics of phase transitions: Theory of Ostwald ripening. Journal of Chemical Physics, 79, 373-378.

Marshall, W.L. and Warakomski, J.M. (1980). Amorphous silica solubilities-II. Effect of aqueous salt solutions at 25°C. Geochimica et Cosmochimica Acta, 44, 915-924.

Miguez, H., Meseguer, F., Lopez, C., Mifsud, A., Moya, J.S., and Vazquez, L. (1997). Evidence of FCC crystallization of SiO2 nanospheres. Langmuir, 13, 6009-6011.

Molins, S., Trebotich, D., Yang, L., Ajo-Franklin, J.B., Ligocki, T.J., Shen, C., and Steefel, C.I. (2014). Pore-scale controls on calcite dissolution rates from flow-through laboratory and numerical experiments. Environmental Science & Technology, 48, 7453-7460.

Putnis, A. and Putnis, C.V. (2007). The mechanism of reequilibration of solids in the presence of a fluid phase. Journal of Solid State Chemistry, 180, 1783-1786.

Pouget, E.M., Bomans, P.H.H., Goos, J.A.C.M., Frederik, P.M., de With, G., and Sommerdijk, N.A.J.M. (2009). The initial stages of template-controlled CaCO3 formation revealed by cryo-TEM. Science, 323, 1455-1458

Reboul, J., Furukawa, S., Horike, N., Tsotsalas, M., Hirai, K., Uehara, H., Kondo, M., Louvain, N., Sakata, O., and Kitagawa, S. (2012). Mesoscopic architectures of porous coordination polymers fabricated by pseudomorphic replication. Nature Materials, 11, 717-723.

Schindelin, J., Arganda-Carreras, I., Frise, E., Kaynig, V., Longair, M., Pietzsch, T., Preibisch, S., Rueden, C., Saalfeld, S., Schmid, B., Tinevez, J.-Y., White, D.J., Hartenstein, V., Eliceiri, K., Tomancak, P., and Cardona, A. (2012). Fiji: an open-source platform for biological-image analysis. Nature Methods, 9, 676-682.

Schmitt, J.G. and Boyd, D.W. (1981). Patterns of silicification in Permian pelecypods and brachiopods from Wyoming. Journal of Sedimentary Research, 51, 1297-1308.

Titiloye, J.O., Parker, S.C., and Mann, S. (1993). Atomistic simulation of calcite surfaces and the influence of growth additives on their morphology. Journal of Crystal Growth 131, 533-545.

Turner, F.J., Griggs, D.T., and Heard, H. (1954). Experimental deformation of calcite crystals. Geological Society of America Bulletin, 65, 883-934.

Williams, L.A. and Crerar, D.A. (1985). Silica diagenesis; II, General mechanisms. Journal of Sedimentary Research, 55, 312-321.

2.7 Supplementary Material

Supplementary Figure 2.1. Silica-replaced bivalve shells and their host rock. **(a)** Pseudomorphic replacement of the shells preserved delicate details, e.g., growth lines. Unsilicified sediment covers the surface of specimens. **(b)** Microphotograph (plane polarized light) of the deeply chemically weathered Cretaceous Bulldog Shale that hosts the silica-replaced bivalve shells. The unsilicified siltstone consists of kaolinite, quartz, hematite, and minor illite. Scale bars: **(a)** 1 cm, **(b)** 500 µm.

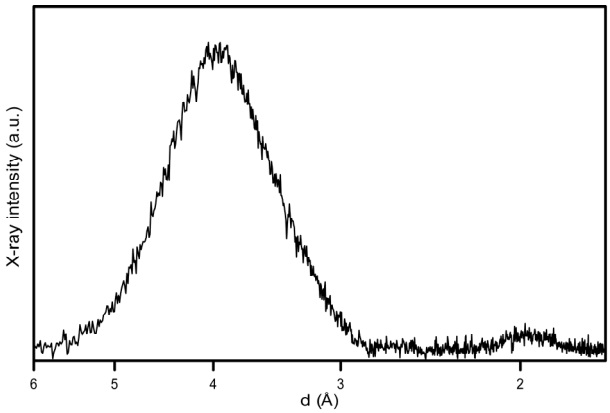

Supplementary Figure 2.2. A representative µ-X-ray diffractrogram of the replacement silica. All diffractograms show a broad reflection centered at ~4 Å, indicative of X-ray amorphous silica (Jones & Segnit 1971). An additional very broad reflection of low intensity occurs at about 2 Å.

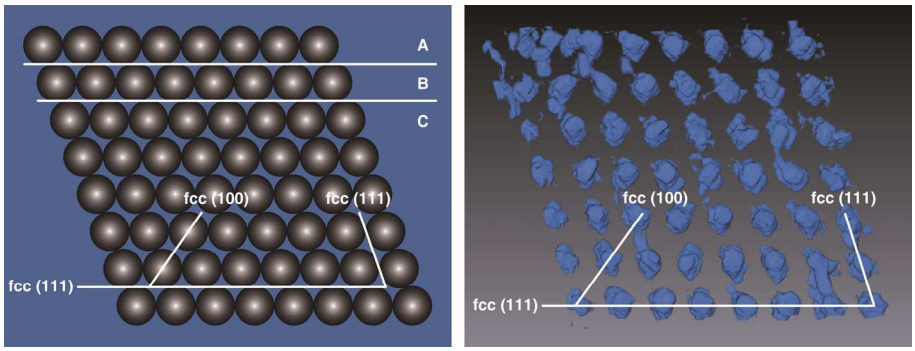

Supplementary Figure 2.3. Sphere and pore arrangement in an ideal (left side) and the observed (right side) face-centered cubic (fcc) lattice, projected along uvw [01-1]. The fcc lattice consists of an A B C A B C ··· stacking sequence of close-packed (111) planes. Two equivalent (111) and a (100) net plane are shown for comparison in both images.

Supplementary Table 2.1. Electron microprobe analysis of the investigated shell samples. DL denotes detection limit.

Oxide (wt %)	Sample number			
	1	2	3	4
SiO_2	90.49	91.10	88.91	90.22
TiO_2	<DL	0.05	0.05	<DL
Al_2O_3	1.31	1.50	1.36	1.59
Fe_2O_3-total	0.06	0.08	0.07	0.14
MnO	<DL	<DL	0.06	0.05
MgO	0.03	0.04	0.04	0.04
CaO	0.36	0.41	0.34	0.46
SrO	0.04	<DL	0.03	<DL
BaO	0.02	0.03	0.08	0.08
Na_2O	0.08	0.20	0.07	0.22
K_2O	0.12	0.19	0.11	0.19
SUM total	92.51	93.60	91.12	92.99
SUM impurities	2.02	2.50	2.21	2.77
Impurities (element wt %)	1.22	1.50	1.32	1.72

Chapter 3

Silica colloid ordering in a dynamic sedimentary environment

Published as:

Liesegang, M. and Milke, R. (2018). Silica colloid ordering in a dynamic sedimentary environment. *Minerals*, 8, 12.

https://doi.org/10.3390/min8010012

3.1 Abstract

The formation of ordered particle arrays plays an essential role in nanotechnology, biological systems, and inorganic photonic structures in the geosphere. Here, we show how ordered arrays of amorphous silica spheres form in deeply weathered lithologies of the Great Artesian Basin (central Australia). Our multi-method approach, using optical and scanning electron microscopy, X-ray microdiffraction, Raman spectroscopy, and electron probe microanalysis, reveals that particle morphologies trace the flow of opal-forming colloidal suspensions and document syn- and post-depositional deformation. The micromorphology of amorphous silica pseudomorphs suggests that the volume-preserving replacement of non-silicate minerals proceeds via an interface-coupled dissolution precipitation process. We conclude that colloid flow and post-depositional shearing create but also destroy natural photonic crystals. Contrary to previous studies, our results indicate that purely gravitational settling/ordering is the exception rather than the rule during the formation of three-dimensional periodic sphere arrays in the highly dynamic colloidal suspensions of chemically weathered clastic sediments.

3.2 Introduction

The hydrated mineralogical assemblages of the Great Artesian Basin (central Australia) record the acidic oxidative weathering of volcaniclastic sediments on a multimillion-year time scale (Rey 2013). Chemical weathering of the silicate rocks induces the *in situ* formation of amorphous silica at silicate mineral surfaces (Thiry et al. 2006) and the release of silica into solution, followed by amorphous nanoparticle precipitation through inorganic processes (Williams & Crerar 1985). Scanning electron microscopy shows that nanosphere-based amorphous silica (opal-A) in central Australia consists of subparticles tens of nanometers in size, indicating aggregative particle growth (Darragh et al. 1966, Gaillou et al. 2008b, Liesegang & Milke 2014, Liesegang et al. 2017). Ordering of the final silica spheres leads to the formation of a natural photonic crystal that modulates visible light due to Bragg diffraction. In precious opal-A, uniform spheres form a regular three-dimensional array that diffracts visible light, giving the characteristic play-of-color (Flörke et al. 1991, Sanders 1964), which is absent in common opal-A.

So far, the formation of ordered sphere lattices in fractures and pores of the host rocks and during mineral replacement has been attributed to gravitational sphere settling (Darragh et al. 1966, Pecover 2007, Gaillou et al. 2008b, Pewkliang et al. 2008, Rey 2013). All of these models agree that gravity and short-range particle interaction potentials create structural order when uniform spheres form in a gel and sediment from or through it at quiescent conditions in sealed environments. This classical theory contrasts considerably with the abundant presence of opal-bearing hydraulic fractures, viscous colloid flow textures, opal reactivation structures, and nanoscale replacement processes in the subsurface precious opal deposits (Pecover 2007, Rey 2013, Liesegang & Milke 2014, Liesegang et al. 2017). These characteristics demonstrate the highly dynamic environment that produces ordered arrays of uniform, X-ray amorphous silica spheres. In this study, we use

a multi-method analytical approach to identify the mineralogical and micromorphological characteristics of these ordered arrays in two different contexts: fracture infilling and replacement. These new data allow us to provide a coherent interpretation of particle ordering processes that are consistent with the dynamic environment. Our results contradict the classical theory of gravitational sphere settling at quiescent conditions in sealed environments.

3.3 Materials and methods

Sample material

Australian opals and their host rocks were collected from the precious opal fields (Fig. 3.1) at Andamooka and Mintabie (South Australia) and analyzed using petrographic microscopy, X-ray microdiffraction, Raman spectroscopy, scanning electron microscopy, and electron probe microanalysis. From a total of 82 samples from Andamooka and 13 samples from Mintabie, we selected 22 and 6 samples, respectively, based on textural and mineralogical characteristics for in-depth analyses. Andamooka opal samples are associated with the deeply weathered early Cretaceous sediments of the Marree Subgroup (Barnes et al. 1992, Rey 2013). Samples were extracted from the bleached Early Cretaceous Bulldog Shale (~20 m beneath the surface) in the Teatree Flat field, which is located about 15 km northwest of the Andamooka Township.

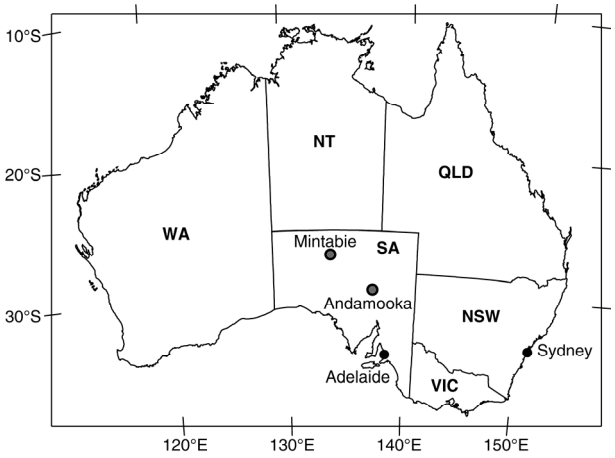

Figure 3.1. Location map of the sample sites in Andamooka and Mintabie (South Australia, Australia).

Silicified sample material from Andamooka comprises silt- and sandstones, conglomerates, and cherts with oolitic structures (Fig. 3.2a). Opaline material fills extensional fractures and pseudomorphically replaces rhombohedral and twinned crystals. The fracture-filling opals from Mintabie are exceptional because they are hosted by tightly cemented, microcline-rich Ordovician sandstone of the Mintabie beds (Fig. 3.2b; Thiry et al. 2006). These samples are typical for the deepest parts of the opal-bearing profiles in the Mintabie field (Thiry et al. 2006). Opals analyzed in this study include gray, milky, white, brown, and transparent samples. Precious opals are transparent with a play-of-color covering the visible spectrum.

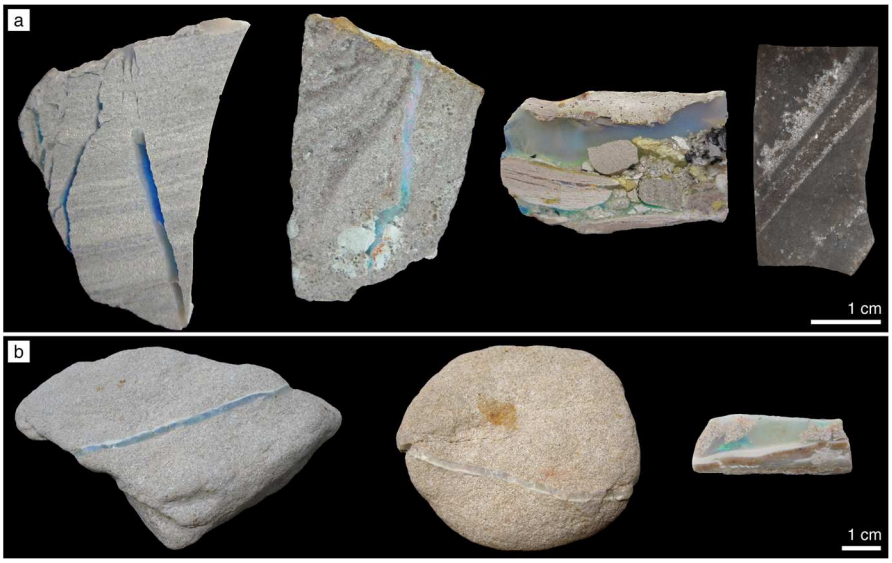

Figure 3.2. Photographs of polished thick sections of samples from Andamooka **(a)** and raw, unprepared sample material from Mintabie **(b)**. **(a)** Andamooka samples, from left to right: opal-filled extensional fractures crosscut the bedding in a bleached sandstone; precious opal in an extensional fracture in sandstone with clay clasts; conglomerate with abundant opal cement and large clasts containing pseudomorphs after carbonates; laminated chert with oolitic structures and opal pseudomorphs after rhombohedral crystals. **(b)** Mintabie samples, from left to right: bleached sandstone with precious and common (white) vein opal; bleached sandstone with predominantly common (white and translucent) vein opal; sandstone fragments in a sample composed of varicolored common opal with minor precious opal domains.

Analytical methods

Diamond-polished thin sections (30 µm thick) and thick sections were prepared using standard procedures. For polarized light microscopy, a Zeiss Axio Lab.A1 petrographic microscope was used. At least 40 intersection angles between thin straight lines in single photonic crystals were measured digitally and averaged. The micromorphology of opals and their host rocks was investigated on the surfaces of thin and thick sections and freshly fractured material by SEM. Specimens were etched in 10 vol % hydrofluoric acid (HF) solution for 15 s, dried, and sputter-coated with ~15 nm W. Secondary electron (SE) images were obtained in a Zeiss Supra 40 VP Ultra SEM instrument (Carl Zeiss, Jena, Germany), at an acceleration voltage of 5 kV and a beam current of 10 nA. Sphere diameters were determined by sizing over 1000 particles from secondary electron images. The sphere diameter dispersity has been calculated as relative standard deviation.

Quantitative element concentrations were determined on carbon-coated, polished thin sections using a JEOL JXA 8200 Superprobe operated at 15 kV accelerating voltage, 20 nA beam current, and a beam diameter of 10 µm. For each opal specimen, 30 point analyses were measured. The acquisition time for Na analysis was 5 s on peak and 5 s on background. The peak and background of other elements were measured for 10 s each. The instrument was internally calibrated using natural silicate, oxide, and basalt (VG-2) and rhyolite (VG-568) glass. Elemental maps were acquired using the WDS detectors. The operating conditions were a 15 kV accelerating voltage and a 20 nA beam current (on Faraday cup), with a beam diameter of 1 µm and a 60 ms counting time per 0.5-1 µm pixel size.

Non-destructive X-ray microdiffraction was used on polished thick sections, at the Eberhard Karls Universität Tübingen (Tübingen, Germany), with a Bruker AXS micro-X-ray diffractometer D8 Discover (Bruker AXS GmbH, Karlsruhe, Germany) with focusing X-ray optics (IfG Berlin, Berlin, Germany; incidence angle of 10°), a HOPG-monochromator, and a large VÅNTEC-500 2D–detector (μ-XRD^2). Diffractograms were recorded for 300 s at a beam diameter of 50 μm in the 2Θ range of 7–67°, using CoKα radiation ($\lambda\alpha_1$ = 1.78897 Å) at 30 kV and a tube current of 30 mA. The step size of the diffractogram was 0.05°2Θ. We analyzed X-ray diffraction patterns with PeakFit 4 (Systat Software, San Jose, CA, USA). After a manual baseline subtraction, we used a five-point Savitzky–Golay moving filter (Savitzky & Golay 1964) to smooth the diffraction pattern and minimize human bias in peak maxima determination. Diffractograms, peak positions, and the full width at half the maximum intensity (FWHM) are expressed as d-spacing (in Å) calculated from the diffraction angles °2θ to facilitate the comparison of diffractograms recorded with different anode material.

Raman spectroscopy analyses were conducted on a Horiba Jobin Yvon LabRAM HR 800 instrument (Horiba Jobin Yvon, Bensheim, Germany) coupled to an Olympus BX41 microscope (Olympus, Hamburg, Germany) at the Museum für Naturkunde (Berlin, Germany). A 785 nm air-cooled diode laser was used to excite the sample with a 100x objective, a spectral integration time of 60 s, and three accumulations. With the Peltier-cooled charge-coupled device (CCD) detector (1024 x 256 pixels), a spectral resolution of ~0.2 cm^{-1}/pixel is achieved. Scattered Raman light was collected in backscattering geometry and dispersed by a grating of 600 grooves/mm after passing through a 100 μm entrance slit. The confocal hole size was set to 1000 μm. Unpolarized spectra were collected with the Labspec 6 software over a range from 100 to 1200 cm^{-1}. An internal intensity correction (ICS, Horiba) was used to correct detector intensities. The instrument was calibrated using the Raman band of silica at 520.7 cm^{-1}.

3.4 Results

Opal mineralogy

We use X-ray microdiffraction and Raman spectroscopy to identify the mineralogy of fracture-filling and replacive opals. The typical X-ray microdiffraction pattern of the studied opals is shown in Figure 3.3a. The diffractograms, expressed as a function of d-spacing, generally show a broad asymmetric peak with a maximum ranging between 3.97 and 4.06 Å and a high d-spacing side shoulder. A secondary broad reflection of low intensity occurs at ~2 Å. The full width at half-maximum intensity (FWHM) of all samples scatters unsystematically from 1.07 to 1.19 Å and is independent of the main peak position. The maximum intensity of the main peak varies unsystematically by less than 5 % between samples. According to the Jones and Segnit (1971) opal classification scheme, the diffractograms of all samples are consistent with those of opal-A. The peak shapes and positions are uniform within individual samples, including those composed of intermingled composites of precious and common opal. Overall, we found no co-variation between peak shapes/positions and the visual appearance, micromorphology, or chemical aspects of the studied material.

Figure 3.3b shows a typical Raman spectrum of the studied opals. The spectra and band maximum positions of opals at all sites are similar and display a prominent band at 425 ± 3 cm^{-1} and bands of lower intensity at 791 ± 1, 961 ± 2, and 1067 ± 3 cm^{-1}. The bands at 425 and 961 cm^{-1} show a positive skewness, while the band at 791 cm^{-1} shows a negative skewness. These asymmetries are likely due to the superposition of separate bands with different shapes and positions. Previous studies assigned the Raman bands at ~425, 791, and 1067 cm^{-1} to fundamental vibrations of the SiO amorphous silica framework (McMillan 1984). The band at ~961 cm^{-1} indicates a Si-OH stretching mode due to silanol groups (Hartwig & Rahn 1977). The Raman spectra of all samples are consistent with those of opal-A (Smallwood et al. 1997) and lack a correlation with the chemical composition, micromorphological features, and peak shapes and positions obtained from X-ray diffraction analyses.

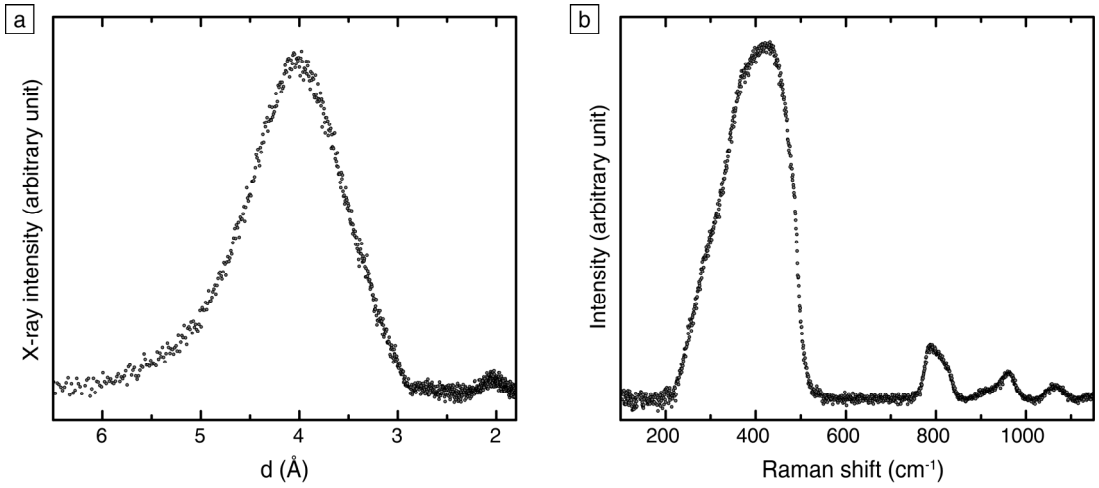

Figure 3.3. A typical X-ray diffractogram **(a)** and Raman spectrum **(b)** of the studied samples. **(a)** X-ray diffraction patterns (plotted as a function of d-spacing calculated from diffraction angles) generally show a broad asymmetric peak with a maximum ranging between 3.97 and 4.06 Å. A smaller, secondary reflection occurs at ~2 Å. **(b)** The Raman spectra of opals studied here show broad asymmetric bands with a maximum at 425 ± 3, 791 ± 1, and 961 ± 2 cm^{-1}, respectively. A more symmetrical band exists at 1067 ± 3 cm^{-1}. All spectra are consistent with opal-A (Smallwood et al. 1997).

Colloid flow structures in fractures

SEM images of vein-filling opal-A show that macroscopic opal characteristics directly link to micromorphological features (Fig. 3.4). Hydraulic extensional fractures contain alternating zones of precious and common opal with variable color and parabolic interfaces pointing toward fracture tips. In these geometries, transparent opals with a play-of-color consist of regularly arranged, uniform spheres ranging in size from 160 to 440 nm. Irregularly arranged spheres with a size of 100–300 nm and minor nonspherical particles form the adjacent translucent common opals. The sphere diameters in translucent common and transparent precious opal are similar (±10 nm) within each sample. The white and milky common opal consists of non-uniform, round to ellipsoidal particles up to 1 µm in length, with a maximum aspect ratio of 0.25. These particles are elongated parallel to the fracture surfaces and parabolic interfaces between adjacent opals. Areas with accumulated, oriented ellipsoidal particles frequently display a moderate first-

order grey birefringence between crossed polarizers (Fig. 3.4d). The sequences of vein-filling opal with parabolic interfaces lack chemical or structural (determined by X-ray microdiffraction and Raman spectroscopy) gradients.

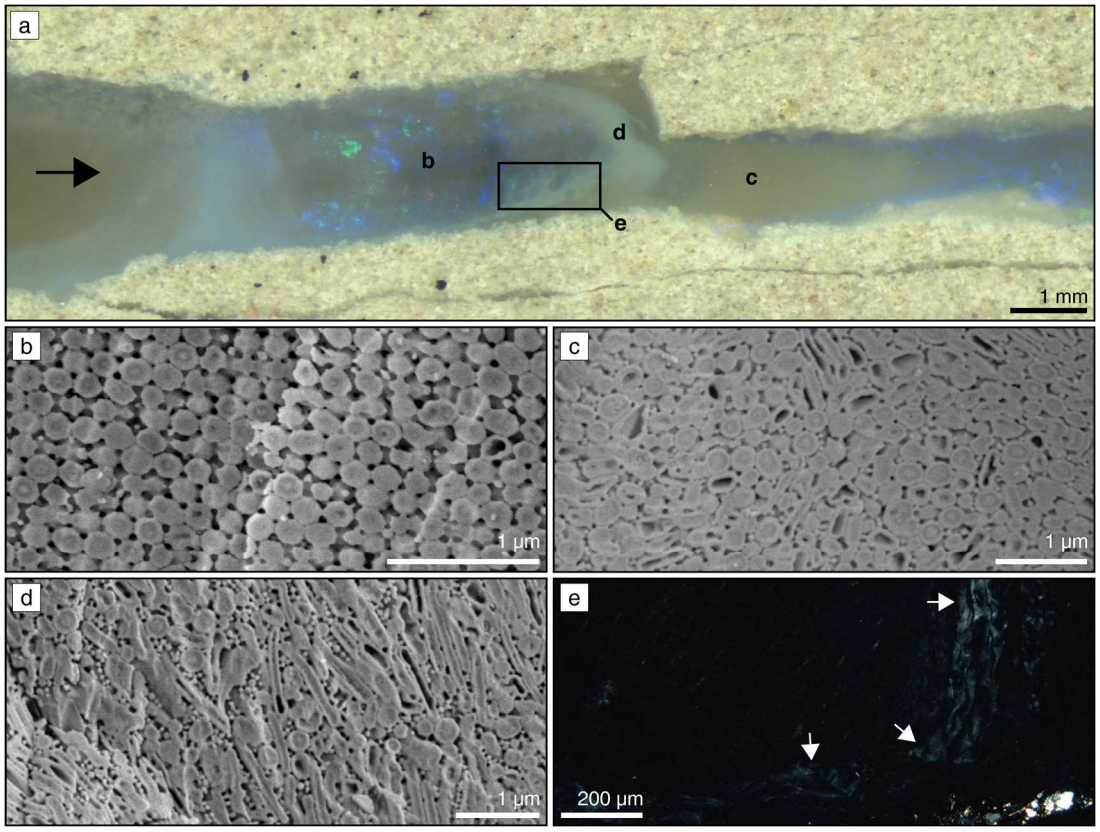

Figure 3.4. Textures and microstructural features of Andamooka vein opal. The SE images **(b-d)** were obtained after HF etching. **(a)** Photograph of alternating zones of transparent precious and translucent to milky common opal. The parabolic interfaces point toward the fracture tip (arrow). **(b)** SE image of precious opal composed of ordered uniform spheres. **(c)** SE image of irregularly arranged spheres and minor nonspherical particles in translucent common opal. **(d)** White to milky common opal composed of ellipsoidal particles with a preferred orientation ~N-S and a maximum aspect ratio of 0.25. **(e)** Microphotograph (crossed polarizers) of the area highlighted in **(a)** depicting the faint grey birefringence of ellipsoidal, ordered particles in white to milky common opal.

The fractures in opal-indurated sandstones of the Mintabie field commonly contain veins of transparent opal intermingled with wave-shaped, layered white opal (Fig. 3.5). These wave features are concentric and resemble unflattened roll-up structures (Eriksson et al. 2000). Minute-sized (<1 µm) kaolinite flakes are embedded in the material and remnants of the host rock are located on its surface. The white opal consists of irregularly arranged, non-uniform spheres <300 nm in diameter and contains randomly scattered, sphere-lined pores, ~0.4 to 3.5 µm in diameter (Fig. 3.5b). These pore architectures are also widespread in the white opal from Andamooka. Wedge-shaped photonic crystals with thin parallel striations and spindle-shaped extensional fractures are located between roll-up structures (Fig. 3.5c). A sharp interface separates the regularly ordered regions from transparent opal composed of dominantly uniform but irregularly arranged spheres (Fig. 3.5d). The chemical composition of the white and transparent opal and the host rock cement varies insignificantly (Table 3.1).

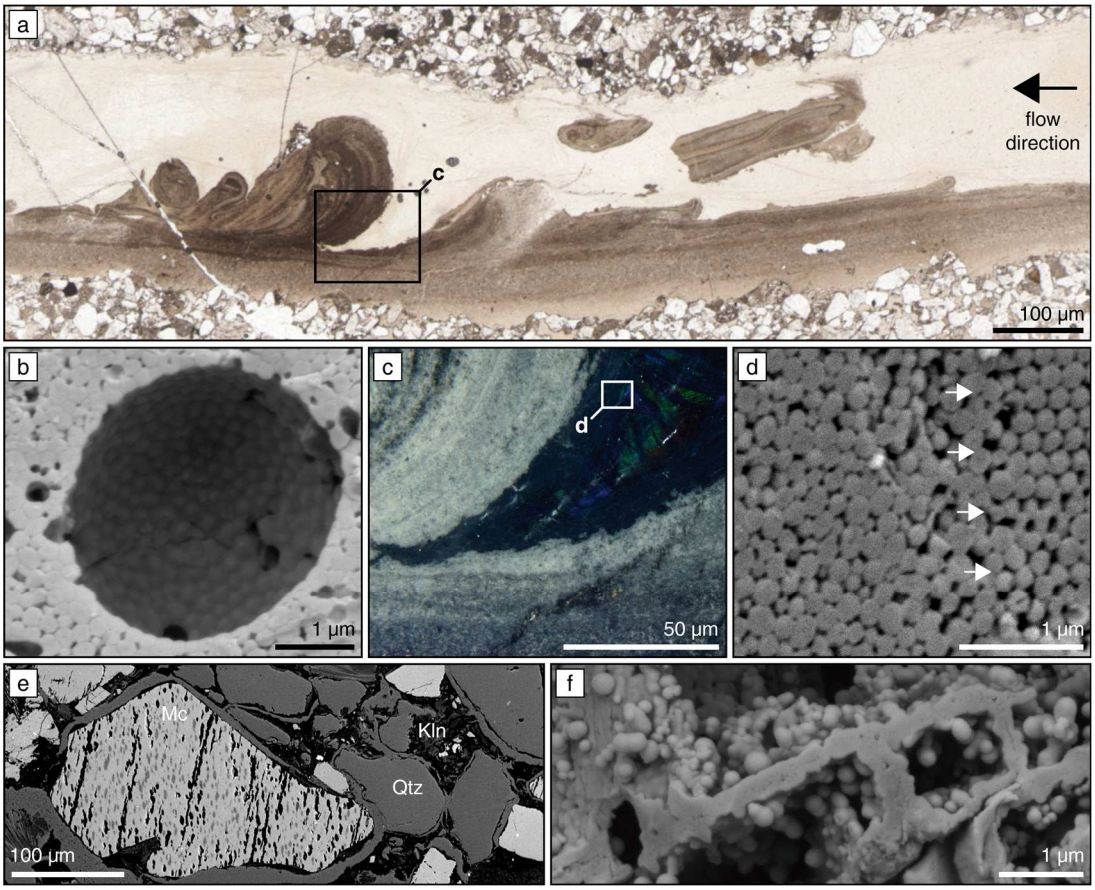

Figure 3.5. Textures and microstructural features of Mintabie vein opal **(a-d)** and its bleached sandstone host rock **(e-f)**. **(a)** Microphotograph of a partially fragmented, brown opal (white in hand specimen) with roll-up structures overlain by transparent common and precious opal. The arrow indicates the flow direction of the concentrated colloid solution that deformed the brown opal. **(b)** SE image of sphere-lined pore space in brown opal in **(a)**, typical of macroscopically white opal at Mintabie and Andamooka. The sample was HF-etched prior to imaging. **(c)** Microphotograph of the area highlighted in **(a)**, showing a wedge-shaped photonic crystal embedded in transparent common opal, between crossed polarizers. **(d)** SE image on HF-etched material of the area highlighted in **(c)**, showing the contact between transparent common and precious opal. Arrows emphasize the interface between disordered (left) and ordered (right) regions of similar-sized spheres. **(e)** Backscattered electron image of bleached Mintabie sandstone with microcline (Mc), quartz (Qtz), and kaolinite (Kln) in their typical spatial context. Microcline and quartz grains are surrounded by an opal-A cement. Na-rich regions (dark) in microcline dissolve preferentially during alteration. **(f)** SE image of an opal-A pseudomorph after microcline with dissolution cavities containing non-uniform spheres <300 nm in diameter. The opal-replaced cavity walls trace microcline cleavage planes.

Table 3.1. Chemical composition of opal-A samples shown in Figures 3.4–3.6 analyzed by electron probe microanalysis (EPMA) (in wt %). The data are averaged from 30 point analyses per sample. Vein opal from Andamooka refers to Figure 3.4. Mintabie opals are shown in Figure 3.5. Replacement opal-A from Andamooka comprises twinned and untwinned crystals shown in Figure 3.6.

Oxide	Andamooka				Mintabie		
	Vein opal	Twinned crystal[1]	Rhombs[1]	Inverse opal	Cement	Transparent	White roll-ups
SiO_2	90.60	92.63	87.90	84.45	90.25	90.72	89.98
TiO_2	0.05	0.06	<LLD	<LLD	0.01	0.03	0.03
Al_2O_3	0.93	1.23	1.40	1.42	1.17	1.13	1.18
Fe_2O_3-total	0.09	0.29	0.10	0.09	0.04	0.07	0.08
MgO	0.04	0.08	0.04	0.04	0.01	0.04	0.04
CaO	0.06	0.12	0.09	0.08	0.14	0.12	0.13
SrO	0.03	0.03	0.02	0.02	0.04	0.03	0.03
BaO	0.09	0.10	0.08	0.06	0.10	0.08	0.09
Na_2O	0.10	0.13	0.29	0.30	0.18	0.17	0.18
K_2O	0.09	0.12	0.09	0.05	0.27	0.26	0.32
SUM Total	92.08	94.79	90.01	86.50	92.21	92.65	92.07
SUM impurities	2.19	2.16	2.11	2.06	1.96	1.93	2.08
(H_2O+OH)[2]	10.73	5.21	9.99	13.50	7.79	7.35	7.93

[1] Precious opal
[2] Calculated by balance of SUM total with 100 wt %.

Mineral replacement structures

Transmitted light microscopy reveals that fractures in silicified siltstones contain an- to subhedral, randomly oriented, optical photonic crystals up to 1.5 mm in size (Fig. 3.6a). Observation between crossed polarizers reveals parallel striations (3–180 µm wide) that mimic polysynthetic twin lamellae on trigonal {018} indicative of recrystallized calcite. The twinned condition of the lamellae is visible as a periodic color variation that changes both color and intensity upon rotation on the microscope stage. The color variations arise from Bragg diffraction effects from close-packed, uniform silica spheres and air-filled pores with rhythmically changing orientation (Fig. 3.6b). The average sphere diameter varies between samples from 200–320 nm (size dispersion <4 %). X-ray microdiffraction, Raman spectroscopy, and elemental mapping confirm the amorphous nature of the opaline material and indicate the absence of crystalline precursor remnants.

Randomly oriented, opal-filled rhombohedra (<120 µm) are abundant in quartz- and opal-cemented cherts containing round to ellipsoidal oolitic structures (Fig. 3.6c-e). These samples are likely reworked fragments of Cambrian age Andamooka Limestone (Carr et al. 1979). The ooids range in size between 200 and 600 µm and are composed of a uniform mosaic of up to 20 µm-sized, interlocked quartz crystals. Small (<2 µm), anhedral dolomite crystals ($Ca_{1.1}Mg_{0.9}(CO_3)_2$ on average) randomly scatter through the quartz

mosaic. In transmitted light, opal rhombohedra resembling dolomite rhombs consist of inclusion-free transparent to brown opal-A with variable micromorphology. A homogeneous amorphous silica veneer (~60 nm) covers the inner surface of the rhombs (Fig. 3.6d). Transparent common opal inside the rhombohedra consists of 200–300 nm large, uniform spheres in a predominantly irregular arrangement. Precious opal is composed of similar-sized, but close-packed spheres. Dark brown rhombohedra consist of inverse opal with a regular arrangement of spherical void spaces surrounded by solid walls of opal-A (Fig. 3.6e).

The sandstones of the Mintabie field contain abundant microperthitic microcline partially or entirely altered to translucent opal and/or kaolinite flakes (Fig. 3.5e-f). Aggregates of submicrometer-sized kaolinite platelets and non-uniform silica spheres 120 to 270 nm in diameter fill the dissolution cavities in relictic feldspar grains. The opal-replaced cavity walls resemble fused spheres and occasionally contain subparticles ~50 nm in diameter.

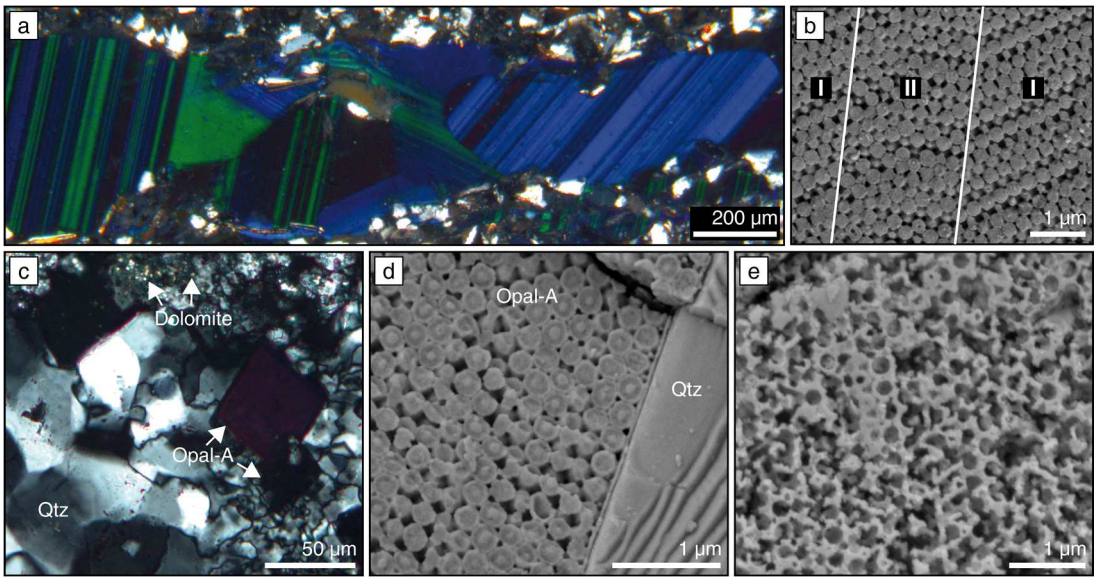

Figure 3.6. Optical photonic crystal pseudomorphs with precursor preservation from Andamooka. The images **(b)** and **(d)** were captured on HF-etched samples. **(a)** Microphotograph of fracture-filling striated photonic crystals with different colors and orientations between crossed polarizers. **(b)** SE image of the polished surface of a twinned crystal with alternating sphere array orientation in an I-II-I pattern. White lines highlight the interface between sphere stacks with different orientation. **(c)** Microphotograph of opal-A-filled rhombs in a quartz-cemented sample with ooids replaced by a mosaic of interlocked quartz crystals and dolomite. **(d)** SE image of the interface between precious opal-A inside rhombs and quartz on the outside as in **(c)**. **(e)** SE image of inverse opal-A in rhombohedral pseudomorphs.

Polyhedral particle shapes and crystal bending

Opal-A from all sample localities consists of silica particles with variable size, shape, ordering, internal structure, and degree of cementation. Close-packed particle arrays often consist of grains with a polyhedral shape (Fig. 3.7a). A mild HF etching of these polyhedral spheres reveals a concentric structure composed of subparticles 20–40 nm in diameter. This subparticle structure is common to all opals studied here, irrespective of their fracture-filling or replacive nature, shape, or chemical composition.

Vein-filling common opal frequently contains anhedral photonic regions with uniform color between crossed polarizers. These crystals often display two sets of intersecting thin black lines less than 1 µm wide (Fig. 3.7b). Straight lines form diamond shapes and intersect at an angle of 70.2 ± 1.1°. However, in most grains, these lines are bent to a variable degree. Locally, the photonic crystals display extensional fractures filled with irregularly arranged spheres.

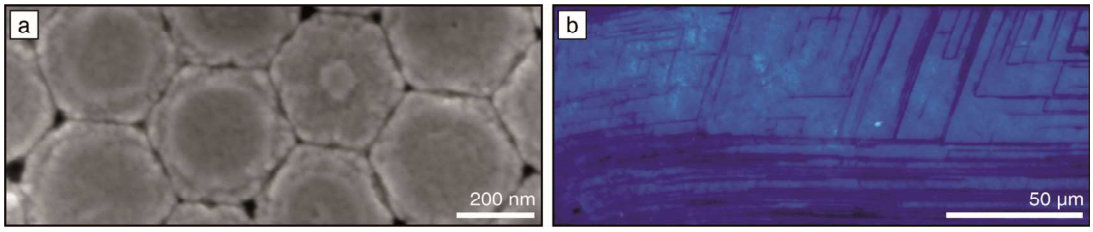

Figure 3.7. Post-depositional deformation features in precious opal from Andamooka. **(a)** Secondary electron image of HF acid-etched, hexagonal particles with concentric layering and subparticle structure. The pore space is significantly reduced compared to close-packed, ideal spheres. **(b)** Microphotograph of an opal-A photonic crystal between crossed polarizers showing thin black lines indicative of lattice displacement. Black lines on the right side intersect at an angle of ~70°. The lines are continuously bent toward the left side.

3.5 Discussion

Scattering of visible light on the microstructurally diverse opal-A studied here creates color profiles that coincide with micromorphological characteristics, e.g., particle ordering and shape. Several authors have suggested that opal forms from a gel (Darragh et al. 1966, Pecover 2007, Gaillou et al. 2008b, Pewkliang et al. 2008, Rey 2013). At quiescent conditions in sealed environments, uniform spheres are expected to grow inside this gel and settle gravitationally to form a regular sphere array, i.e., precious opal. However, such a gel matrix strongly immobilizes particles (Dickinson 2013), impeding sphere growth, mobility, and arrangement into ordered arrays. Additionally, later particle mobility requires extensive breaking of interparticle bonds (Iler 1979). These restrictions equally apply to fracture-filling and replacive opal. In fact, the textural properties of the opals studied here and the aggregative grown single-particle structure point to precipitation and growth of spheres as free units in a sol rather than a gel. After sphere arrangement, dissolved silica from bulk solution or subparticle breakdown precipitates on the available surfaces and acts as a cementing agent (Sanders 1964, Carcouët et al. 2014).

Flow-induced ordering

The uniform direction of parabolic fronts in the vein opal indicates that fluid flow directs particles along a pressure gradient toward the fracture tip. The parabolic shape of the opal fronts resembles turbulent non-Newtonian flow velocity profiles (Peixinho et al. 2005) and indicates a strong coupling between colloid flow and structural ordering. This observation agrees well with non-Newtonian fluid flow textures preserved in vein opals in previous studies (Pecover 2007, Rey 2013). Apparently, colloid flow results in a hierarchy of particle packing, orientation, and deformation.

The uniform diameter of spherical particles in individual vein opal samples indicates that deformation occured when the spheres grew to their final size but were still deformable. The similar chemical composition, microdiffraction and Raman spectroscopic properties, and size of spherical particles point to a pre-existent reservoir of uniform spheres that entered the fracture upon opening. Nonspherical particle morphologies would form within this reservoir only under highly localized, substantially different physicochemical conditions (Ding et al. 2014). During colloid ingress into the opening fracture, the pressure gradient forces the particles toward the fracture tip. The increase in particle number within the spatially restricted volume results in a local increase of the fluid's viscosity and jamming of the particles without fusion of the spheres. The flow leads to structuring of the concentrated colloidal suspension and directional ordering of nonspherical particles. The birefringent character of parabolic fronts between crossed polarizers results from the flow-induced uniform orientation of flattened but regularly ordered particles (Hong et al. 2015).

The texture of Mintabie vein opals illustrates how a flowing colloidal suspension reactivates and deforms opaline structures. It is probable that the concentric roll-ups reflect re-orientation of earlier-formed opal by the current activity of the colloidal suspension. The structure of the reactivated opaline material suggests that the viscosity of this suspension was high enough to induce roll-up structures in cohesive material and keep ripped-up material suspended. Wedge-shaped photonic structures between roll-up structures (Fig. 3.5) contradict a gravitational sphere settling and ordering process, because gravitational settling likely results in horizontally layered photonic structures with a similar orientation. Previous studies have suggested that composite gels with ordered and unordered domains migrate under differential pressure and preserve their structural order (Rey 2013). Accordingly, ordered domains should initially possess a complex wedge shape and orientation that fit its final position. However, ordered sphere lattices with a comparable shape are absent from all fracture-filling opal in the present study. This might indicate that the sphere lattice of wedge-shaped photonic regions results from a flow-induced sphere ordering process, analogous to the shear-induced ordering of a disordered colloidal suspension (Vermant & Solomon 2005, Wu et al. 2009). Thus, fluid flow locally transports the spheres into the correct position to create ordered lattices.

Mineral replacement

Apart from the textural similarities of vein opals, the highly selective replacement of carbonate and clay minerals, wood, gypsum, fossils, and organic material by opal-A is frequently reported (Scurfield & Segnit 1984, Barnes et al. 1992, Rey 2013, Liesegang & Milke 2014). To date, the replacement of silicates and carbonate fossils by precious opal-A has been attributed to the infilling of cavities, resulting from partial or bulk dissolution, by a silica-rich gel (Pewkliang et al. 2008, Rey 2013). This gel matrix inhibits particle growth and requires considerable bond breaking, analogous to the sphere-forming processes in fractures. Additionally, the pseudomorphs studied here lack evidence for the shrinkage or layering that may indicate

gel desiccation or changes in gel composition (Pewkliang et al. 2008), respectively. These restraints imply that another process induces structural order during pseudomorphic replacement.

The twinned photonic crystals evidence that carbonate replacement is intimately coupled to the precursor crystallographic orientations. Replacement along lattice planes of the precursor crystal ensures the constant physicochemical conditions that are required for uniform sphere sizes, shapes, and arrays (Liesegang et al. 2017). The dissolution reaction creates a sharp localized pH and salinity increase (Molins et al. 2014) that gradually decreases toward the bulk fluid. This local change lowers the amorphous silica solubility, induces supersaturation and precipitation (Iler 1979), and confines particle nucleation close to the moving calcite dissolution front. In this interface-coupled dissolution-precipitation process (Putnis & Putnis 2007, Liesegang et al. 2017) the precursor dissolution and silica deposition fronts advance synchronously. During the replacement process, silica nanoparticles continuously nucleate, aggregate, and form close-packed planes parallel to the most stable lattice planes of the crystalline template (Fig. 3.8). The particle size increases at increasing distance from the dissolution front. The nanoporous close-packed sphere geometry (~26 % porosity) is permissive and enables mass transport and permanent fluid access to the calcite dissolution front. The textures and random orientation of the crystal pseudomorphs indicate that gravitational settling is negligible in this case. Our observations further show that carbonate precipitation in extensional fractures locally precedes precious opal formation.

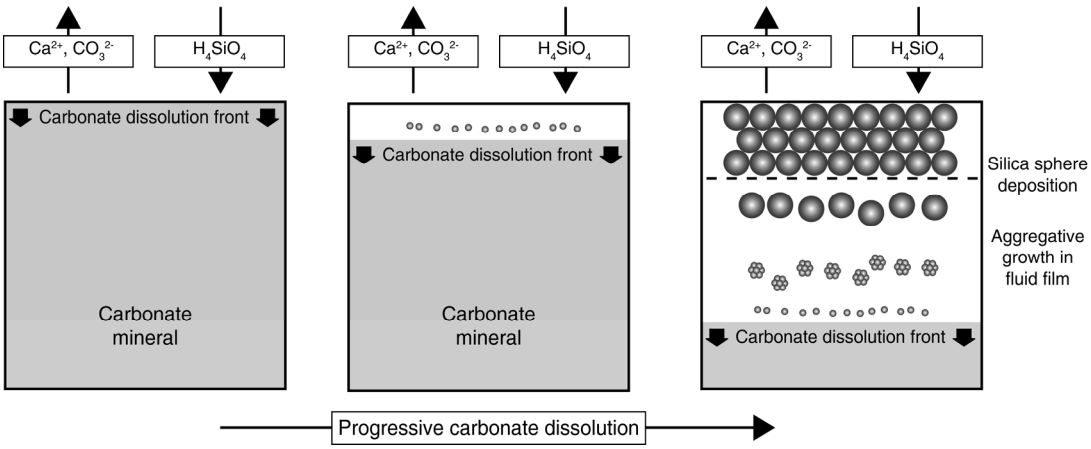

Figure 3.8. Schematic representation of the volume- and texture-preserving replacement process of a carbonate mineral by amorphous silica nanospheres. Carbonate chemical components are constantly removed into the bulk solution, while dissolved silica (H_4SiO_4) reaches the carbonate surface. Amorphous silica nanoparticles continuously nucleate close to the carbonate surface, aggregate into larger particles in the interfacial fluid film, and self-assemble into close-packed, hexagonal planes. The particle diameter increases at increasing distance from the dissolution front until they reach their final size. The carbonate dissolution and silica deposition fronts advance synchronously during the interface-coupled dissolution-precipitation process. The final spheres form a long-range ordered photonic crystal.

Preservation of twin structures in photonic crystal assemblies appears to be a reliable indicator for a replacive interface-coupled dissolution-precipitation mechanism, but the replacement of untwinned crystals is not as straightforward. We observe that randomly oriented rhombohedra consist of ordered uniform spheres. Gravitational sphere settling may fill pseudomorphs but will result in irregular rim structures,

horizontal layering, and a late, disordered horizontal region due to limited late-stage particle mobility. Partial infilling of pore space may indicate bulk dissolution of the precursor material. Precious opal in the rhombohedral pseudomorphs studied here lacks all these microstructural features. More likely, close-packed sphere arrays in pseudomorphs predominantly form by an interface-coupled dissolution-precipitation process. This process creates the structural perfection of replacive precious opal compared to those formed by sphere sedimentation.

Generally, the microstructure differs between pseudomorphs after silicate minerals (e.g., feldspar) and non-silicates (e.g., carbonate and sulfate minerals). While close-packed sphere arrays replace carbonates and sulfates (Thiry et al. 2006, Liesegang et al. 2017), pseudomorphs after feldspar consist of non-uniform spheres in dissolution cavities (Figure 3.5f). These pseudomorphs are the porous products of the short distance transport and polymerization of dissolved silica. This silicate replacement process does not produce precious opal, due to the small volume fraction of spheres, unless an external source provides additional silica in solution.

Post-depositional lattice deformation

Dislocations and polyhedral particle shapes in ordered sphere arrays indicate post-depositional deformation (Fig. 3.7). At a small shear force, the deformation of soft, ordered spheres into polyhedra decreases pore space and induces a blue-shift of the diffracted light (Sun et al. 2005). Therefore, sheared sphere arrays may preserve their long-range order but lose their optical photonic character. At higher shear forces, colloidal crystals can form dislocations or break (Imhof et al. 1994). Previous studies have shown that dislocations in face-centered cubic (fcc) sphere arrays are visible as permanently extinct lines between crossed polarizers (Rey 2013, Liesegang et al. 2017). This microscopic observation results from isotropic light scattering on the locally imperfect structure. In the present study, straight, extinct lines intersect at an angle of 70.2 ± 1.1° in untwinned photonic crystals. This intersection angle compares closely with those of ideal fcc {111} planes at 70.53°. Apparently, fcc {111} planes are the preferred slip planes in the natural fcc crystals. Further deformation induces bending and partial disintegration of the crystals. As the wavelength of diffracted light depends on crystal orientation (Monovoukas & Gast 1991), deformation may result in lattice re-orientation and an undulose color of the crystal.

3.6 Acknowledgments

Funding for this research was provided by the German Research Council (DFG), grant number MI1205/5-1. We thank Jürgen Ganzel, Berlin, for supplying the samples. Christoph Berthold (Eberhard Karls Universität Tübingen, Germany) provided access to µ-X-ray facilities. Tanja Mohr-Westheide (Naturkundemuseum, Berlin, Germany) provided access to the Raman spectrometer. We acknowledge support by the Open Access Publication Fund of the Freie Universität Berlin.

3.7 References

Barnes, L.C., Townsend, I.J., Robertson, R.S., and Scott, D.C. (1992). Opal: South Australia's gemstone (Handbook No. 5); Department of Mines and Energy, Geological Survey of South Australia: Parkside, South Australia, Australia.

Carcouët, C.C.M.C., van de Put, M.W.P., Mezari, B., Magusin, P.C.M.M., Laven, J., Bomans, P.H.H., Friedrich, H., Esteves, A.C.C., Sommerdijk, N.A.J.M., van Benthem, R.A.T.M., and de With, G. (2014). Nucleation and growth of monodisperse silica nanoparticles. Nano Letters, 14, 1433-1438.

Carr, S.G., Olliver, J.G., Conor, C.H.H., and Scott, D.C. (1979). Andamooka opal fields: The geology of the precious stones field and the results of the subsidised mining program. Report of Investigations 51, Department of Mines and Energy, Geological Survey of South Australia: Adelaide, Australia, 1979; pp. 17-18. ISBN 0724354980

Darragh, P., Gaskin, A., Terrell, B., and Sanders, J. (1966). Origin of precious opal. Nature, 209, 13-16.

Dickinson, E. (2013). Structure and rheology of colloidal particle gels: Insight from computer simulation. Advances in Colloid and Interface Science, 199, 114-127.

Ding, T., Long, Y., Zhong, K., Song, K., Yang, G., and Tung, C.H. (2014). Modifying the symmetry of colloidal photonic crystals: a way towards complete photonic bandgap. Journal of Materials Chemistry C, 2, 4100-4111.

Eriksson, P.G., Simpson, E.L., Eriksson, K.A., Bumby, A.J., Steyn, G.L., and Sarkar, S. (2000). Muddy roll-up structures in siliciclastic interdune beds of the c. 1.8 Ga Waterberg Group, South Africa. Palaios, 15, 177-183.

Flörke, O.W., Graetsch, H., Röller, K., Martin, B., and Wirth, R. (1991). Nomenclature of micro-and non-crystalline silica minerals, based on structure and microstructure. Neues Jahrbuch für Mineralogie, Abhandlungen, 163, 19-42.

Gaillou, E., Fritsch, E., Aguilar-Reyes, B., Rondeau, B., Post, J., Barreau, A., and Ostroumov, M. (2008). Common gem opal: An investigation of micro- to nano-structure. American Mineralogist, 93, 1865-1873.

Hartwig, C.M. and Rahn, L.A. (1977). Bound hydroxyl in vitreous silica. The Journal of Chemical Physics, 67, 4260-4261.

Hong, S.H., Shen, T.Z., and Song, J.K. (2015). Flow-induced alignment of disk-like graphene oxide particles in isotropic and biphasic colloids. Molecular Crystals and Liquid Crystals, 610, 68-76.

Iler, R.K. (1979). The Chemistry of Silica: Solubility, polymerization, colloid and surface properties, and biochemistry; Wiley: New York, USA.

Imhof, A., van Blaaderen, A., and Dhont, J.K.G. (1994). Shear melting of colloidal crystals of charged spheres studied with rheology and polarizing microscopy. Langmuir, 10, 3477-3484.

Jones, J.B. and Segnit, E.R. (1971). The nature of opal I. Nomenclature and constituent phases. Journal of the Geological Society of Australia, 18, 37-41.

Liesegang, M. and Milke, R. (2014). Australian sedimentary opal-A and its associated minerals: Implications for natural silica sphere formation. American Mineralogist, 99, 1488-1499.

Liesegang, M., Milke, R., Kranz, C., and Neusser, G. (2017). Silica nanoparticle aggregation in calcite replacement reactions. Scientific Reports, 7, 14550.

McMillan, P. (1984). Structural studies of silicate glasses and melts-applications and limitations of Raman spectroscopy. American Mineralogist, 69, 622-644.

Molins, S., Trebotich, D., Yang, L., Ajo-Franklin, J.B., Ligocki, T.J., Shen, C., and Steefel, C.I. (2014). Pore-scale controls on calcite dissolution rates from flow-through laboratory and numerical experiments. Environmental Science & Technology, 48, 7453-7460.

Monovoukas, Y. and Gast, A.P. (1991). A study of colloidal crystal morphology and orientation via polarizing microscopy. Langmuir, 7, 460-468.

Pecover, S.R. (2007). Australian Opal Resources: Outback Spectral Fire. Rocks & Minerals, 82, 102-115.

Peixinho, J., Nouar, C., Desaubry, C., and Théron, B. (2005). Laminar transitional and turbulent flow of yield stress fluid in a pipe. Journal of Non-Newtonian Fluid Mechanics, 128, 172-184.

Pewkliang, B., Pring, A., and Brugger, J. (2008). The formation of precious opal: Clues from the opalisation of bone. Canadian Mineralogist, 46, 139-149.

Putnis, A. and Putnis, C.V. (2007). The mechanism of reequilibration of solids in the presence of a fluid phase. Journal of Solid State Chemistry, 180, 1783-1786.

Rey, P.F. (2013). Opalisation of the Great Artesian Basin (central Australia): an Australian story with a Martian twist. Australian Journal of Earth Sciences, 60, 291-314.

Sanders, J.V. (1964). Colour of precious opal. Nature, 204, 1151–1153.

Savitzky, A. and Golay, M. J. (1964). Smoothing and differentiation of data by simplified least squares procedures. Analytical Chemistry, 36, 1627-1639.

Scurfield, G. and Segnit, E. (1984). Petrifaction of wood by silica minerals. Sedimentary Geology, 39, 149-167.

Smallwood, A.G., Thomas, P.S., and Ray, A.S. (1997). Characterisation of sedimentary opals by Fourier transform Raman spectroscopy. Spectrochimica Acta A, 53, 2341-2345.

Sun, Z.Q., Chen, X., Zhang, J.H., Chen, Z.M., Zhang, K., Yan, X., Wang, Y.F., Yu, W.Z., and Yang, B. (2005). Nonspherical colloidal crystals fabricated by the thermal pressing of colloidal crystal chips. Langmuir, 21, 8987-8991.

Thiry, M., Milnes, A.R., Rayot, V., and Simon-Coinçon, S. (2006). Interpretation of palaeoweathering features and successive silicifications in the Tertiary regolith of Inland Australia. Journal of the Geological Society, 163, 723-736.

Vermant, J. and Solomon, M.J. (2005). Flow-induced structure in colloidal suspensions. Journal of Physics: Condensed Matter 2005, 17, R187-R216.

Williams, L.A. and Crerar, D.A. (1985). Silica diagenesis; II, General mechanisms. Journal of Sedimentary Research, 55, 312-321.

Wu, Y.L., Derks, D., van Blaaderen, A., and Imhof, A. (2009). Melting and crystallization of colloidal hard-sphere suspensions under shear. Proceedings of the National Academy of Sciences, 106, 10564-10569.

Chapter 4

Amorphous silica maturation in chemically weathered clastic sediments

Published as:

Liesegang, M., Milke, R., and Berthold, C. Amorphous silica maturation in chemically weathered clastic sediments. *Sedimentary Geology*, 365, 54-61.

https://doi.org/10.1016/j.sedgeo.2018.01.001

Chapter 5

Conclusions

Ordering from the atomic to centimeter scale

Amorphous silica precipitation and mineralogical maturation play a key role in virtually all surface and subsurface environments of the Earth system. This thesis aims to enhance our understanding of three-dimensional order of amorphous silica on the level of colloidal and atomic dimensions. Based on the combination of field observations, nanoscale morphology, mesoscale geometry, and established concepts from silica synthesis and modeling, I am able to provide coherent models to explain the three-dimensional long-range ordering of amorphous silica nanoparticles. Figure 5.1 summarizes and compares the results of this thesis to the old conceptual model for particle formation and ordering in opal-A. Overall, the results of this work challenge the traditional sphere ordering model prevailing in opal research for the past 50 years. Further, this thesis clarifies the role of nanocrystalline domain growth during the early stage of amorphous silica diagenesis and provides an X-ray diffraction pattern parameter to track the mineralogical transformation of metastable silica.

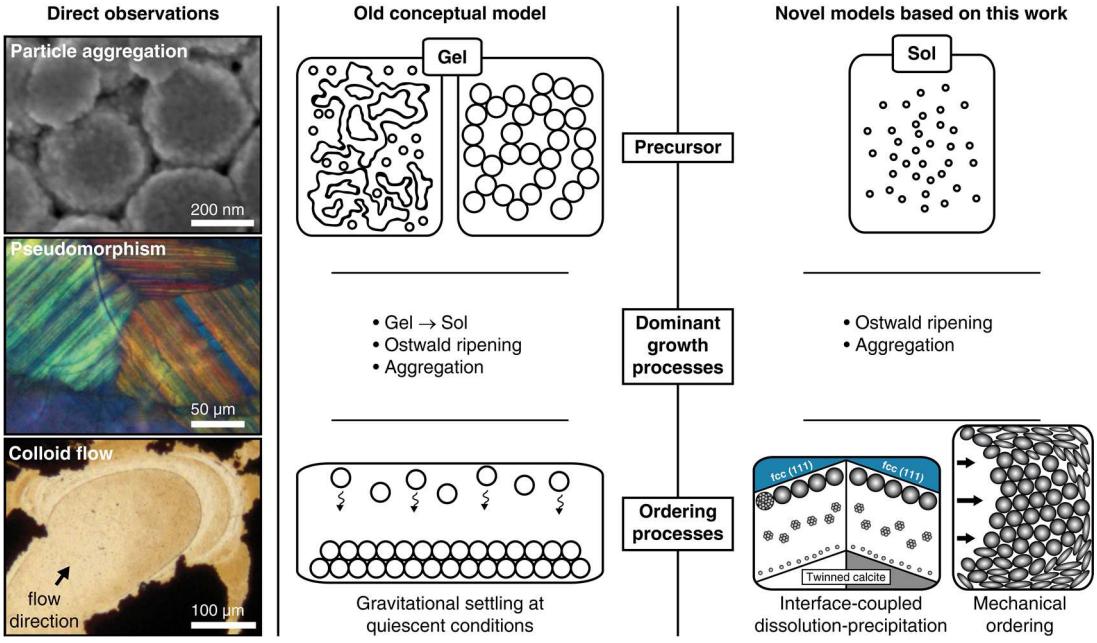

Figure 5.1. Comparison of the old conceptual model for silica particle ordering in nature and the novel models based on direct observations described in this thesis. The precursors and ordering processes are presented two-dimensionally. In the traditional model, gelling of polymers or colloidal dispersions is essential for silica sphere formation. A subsequent gel-to-sol transformation is necessary to create the final spheres that settle gravitationally. The novel models originate from direct observational evidence and show that gelling and purely gravitational settling/ordering are the exception rather than the rule during the formation of ordered sphere lattices.

Analyzing the replacive interaction between two materials ubiquitous in nanotechnology and the Earth system – carbonate minerals and amorphous silica – improves our understanding of the role of nanoparticulate matter in fluid-mediated replacement reactions. In bivalve shells, extensional fractures, and cherts, amorphous silica nanospheres replace dolomite and twinned calcite crystals via an interface-coupled dissolution-precipitation reaction. The resultant photonic crystals form via continuous nanoparticle aggregation and subsequent arrangement into energetically favorable face-centered cubic lattices. These

findings demonstrate that volume-preserving replacement by silica sphere lattices is incompatible with the traditional concept of silica gel infilling cavities. I conclude in a novel model that the replacement process proceeds via a nanoparticle-based, nonclassical crystallization route. To my knowledge, this is the first model that links the recently emerging areas of interface-coupled dissolution-precipitation reactions and crystal growth by particle attachment. The potential applications cover solid-solid phase changes ranging from natural mineral interfaces to the controllable synthesis of three-dimensionally ordered functional materials. The mechanism proposed here is a significant conceptual advance in our understanding of the role and dynamics of nanoparticles in fluid-mediated replacement reactions. I anticipate that this concept will lead to improvements in our knowledge of crystallization from initially nanocolloidal phases (e.g., during dolomitization or fossilization) and synthesis of template-based, self-assembled materials.

Hydraulic fracturing and viscous flow structures in opal-A-bearing veins are omnipresent in the Australian opal fields. These structures indicate a dynamic environment that creates three-dimensional order on the level of colloidal dimensions. Electron and transmitted light microscopy reveal that silica particle morphologies trace the flow of opal-forming colloidal suspensions and document syn- and post-depositional deformation. Remobilization of opaline material and parabolic interfaces in varicolored vein opals indicate non-Newtonian flow of a viscous suspension along a pressure gradient. This colloid flow substantially modifies the structural order of deformable particles in solution and ordered arrays. These results demonstrate that mechanical ordering processes are consistent with field observations and contradict the classical theory of slow gravitational particle settling at quiescent conditions. Post-depositional deformation of ordered spheres creates polyhedral particle shapes, decreases pore volume, and induces a blue-shift of the diffracted light. Microscopic observation shows that linear features in photonic crystals result from isotropic light scattering on the locally imperfect structure of dislocated spheres. From the angular relation of these dislocation features I conclude that close-packed lattice planes are the preferred slip planes in fcc lattices of natural silica photonic crystals. Overall, I find that colloid flow and post-depositional shearing create but also destroy order on the level of colloidal dimensions.

The three-dimensional order on the level of atomic dimensions increases during the early-diagenetic maturation of amorphous silica. I demonstrate that growing low-tridymite/cristobalite nanodomains significantly modify opal-A diffraction patterns, and introduce a parameter to trace the early-stage opal-A to opal-CT transition based on diffraction pattern asymmetry. I identify a positive and almost linear correlation between peak shapes and positions toward more crystalline opal phases. Heating experiments and calculated diffractograms evidence that nucleation and growth of low-tridymite/cristobalite nanodomains in an amorphous matrix induce the peak shifts and symmetry modifications we observe in opal-A diffraction patterns. These results show that XRD analysis is sensitive to the post-depositional state of amorphous silica and that the new asymmetry parameter serves as a valuable tool to track mineralogical maturation. This finding changes the interpretation of amorphous silica X-ray diffraction patterns with respect to the mineralogical early-stage transition between metastable opaline phases. I present an asymmetry

parameter that allows drawing a distinction between natural opal-A samples, so far undetected even with more sensitive analytical methods, for example, Raman spectroscopy. Consideration of sub-nanometer dissolution-reprecipitation processes during diagenesis of metastable amorphous silica will improve our understanding of isotope and trace element cycling deduced from stable silica. Based on the identification of gradual nanodomain growth in the early stage of opal-A diagenesis, the modern mineralogical opal nomenclature may require adjustment.

Der Lebenslauf ist in der Online-Version aus Gründen des Datenschutzes nicht enthalten

Acknowledgments

I first thank my advisor, Ralf Milke, who was an incredibly available and supportive mentor prior to and throughout my time as a PhD student. The work presented here was a team effort. My special thanks go to Jürgen Ganzel. Without his continuous supply of sample material and enthusiasm, this thesis would not have been possible. Further, I thank my co-authors, whose contributions made this project a success. Scientists and technicians at the FU, GFZ, Tübingen University, Uni Basel, ETH Zürich, and Museum für Naturkunde are sincerely thanked for their time and lab resources, scientific advice, and personal input. My family and friends have been a continuous supply of support and life advice outside the science bubble. This helped me to realize this project in the development phase and afterwards. Extensive discussions about the "so what" and "who cares" of this study have encouraged me in my efforts to study and understand the beauty of nature. I thank Esther Schwarzenbach for her invaluable patience and support during the past years. The members of the Mineralogy-Petrology group made my studies possible and delightful.